Table 4 Multivariate logistic regression analysis to identify possible factors related to the development of acneiform rash and xerosis during the first 6 weeks of treatment with erlotinib plus gemcitabine

Factors	Acneiform rash		Xerosis	
	OR (95 % CI)	*p* value	OR (95 % CI)	*p* value
Minocycline treatment				
Prophylactic	0.16 (0.06–0.46)	<0.001	0.11 (0.01–0.90)	0.04
Deferred	1		1	
Gender				
Female	0.30 (0.11–0.87)	0.03		
Male	1			
Erlotinib dose intensity (%)				
<83.3	0.61 (0.23–1.65)	0.30		
≥83.3	1			
UICC disease stage				
III	4.05 (0.94–17.53)	0.06		
IV	1			
ECOG PS				
≥2	1.54 (0.62–3.83)	0.35		
0–1	1			
CEA (ng/mL)				
<5.25			0.50 (0.12–2.10)	0.34
≥5.25			1	

CEA carcinoembryonic antigen, *CI* confidence interval, *ECOG PS* Eastern Cooperative Oncology Group performance status, *OR* odds ratio, *UICC* Union for International Cancer Control

vertigo, and liver dysfunction, known adverse events associated with minocycline treatment. Therefore, our results suggest that long-term treatment with 200 mg/day minocycline, which is the generally used dose around the world, was effective and feasible in patients with advanced pancreatic cancer undergoing treatment with erlotinib plus gemcitabine. In addition, no significant difference was observed in response rate, disease control rate, or PFS between the prophylactic and the deferred minocycline treatment groups in this study. Thus, prophylactic minocycline treatment did not appear to have a significant impact on the anti-tumor effects of erlotinib plus gemcitabine.

Two studies have shown the anti-inflammatory effects of tetracycline following systemic administration [5, 6]. In particular, the open-label phase II STEPP (Skin Toxicity Evaluation Protocol with Panitumumab) trial reported the most persuasive results [6]. It demonstrated that prophylactic skin treatment with a skin moisturizer, sunscreen, topical steroid, and oral doxycycline significantly reduced the incidence of grade 2 or worse skin toxicities compared with the deferred treatment group in metastatic colorectal cancer patients treated with panitumumab (29 vs. 62 %; OR 0.3; 95 % CI 0.1–0.6). Because the prophylactic skin treatment in the STEPP trial included various skincare agents, it is impossible to evaluate the individual efficacy of each of these skincare agents. On the other hand, we could evaluate the efficacy of prophylactic minocycline treatment, because the only difference between the prophylactic and deferred minocycline treatment groups was in the use of minocycline. However, this study was a small, non-randomized, retrospective comparative study, and the patient groups were not concurrently treated. Our results may not be generalizable to the entire patient population because of the single-center setting of the study. A well designed, randomized controlled trial of minocycline is mandatory to evaluate the effects of tetracyclines for the skin toxicities induced by erlotinib in patients with pancreatic cancer.

This retrospective study demonstrated the effectiveness of prophylactic oral minocycline treatment for preventing the development of acneiform rash and xerosis during treatment with erlotinib and gemcitabine in patients with advanced pancreatic cancer; however, the treatment failed to prevent the development of paronychia. A few case reports suggest the efficacy of doxycycline for the treatment of paronychia induced by EGFR inhibitors [20]; however, no randomized controlled trials have shown the efficacy of tetracycline for preventing paronychia induced by EGFR inhibitors. Therefore, there is a need to establish therapies for paronychia in the future.

In our study, and consistent with previous reports, multivariate analysis identified female gender as a significant independent factor associated with the incidence of acneiform rash [9, 21]. Migliaccio et al. [22, 23] reported that activation of Src triggered by androgens induces EGFR phosphorylation. This hormonal action may be one of the reasons for the difference in the incidence of acneiform rash between male and female patients.

Table 5 Treatment-emergent toxicities occurring during the first 6 weeks of treatment with erlotinib plus gemcitabine

Variables	Prophylactic minocycline treatment		Deferred minocycline treatment		*p* value (any grade)	*p* value (grade ≥3)
	Any	Grade ≥3	Any	Grade ≥3		
Any toxicity	44 (100)	25 (56.8)	52 (100)	36 (69.2)	–	0.21
Hematologic						
Leukocytes	41 (93.2)	12 (27.3)	47 (90.4)	16 (30.8)	0.46	0.71
Neutropenia	39 (88.6)	18 (40.9)	44 (84.6)	23 (44.2)	0.24	0.74
Hemoglobin	31 (70.5)	4 (9.1)	42 (80.8)	10 (19.2)	0.60	0.16
Platelets	35 (79.6)	4 (9.1)	39 (75.0)	5 (9.6)	0.61	0.61
Non-hematologic						
Nausea	26 (59.1)	0 (0)	24 (46.2)	0 (0)	0.21	–
Vomiting	9 (20.5)	0 (0)	7 (13.5)	0 (0)	0.36	–
Diarrhea	14 (31.8)	0 (0)	16 (30.8)	0 (0)	0.91	–
Fatigue	29 (65.9)	2 (4.6)	31 (59.6)	1 (1.9)	0.53	0.44
Vertigo	3 (6.8)	0 (0)	1 (1.9)	0 (0)	0.25	–
ILD-like syndrome	2 (4.6)	0 (0)	5 (9.6)	1 (1.9)	0.15	0.54
Biochemical						
AST	28 (63.6)	6 (13.6)	32 (61.5)	7 (13.5)	0.83	0.98
ALT	23 (52.3)	6 (13.6)	29 (55.8)	8 (15.4)	0.73	0.81
Bilirubin	18 (40.9)	4 (9.1)	22 (42.3)	4 (7.7)	0.89	0.55
ALP	16 (31.8)	1 (2.3)	19 (36.5)	0 (0)	0.63	0.46
Creatinine	14 (31.8)	0 (0)	21 (40.4)	0 (0)	0.39	–

Data are presented as *n* (%) unless otherwise indicated

ALP alkaline phosphatase, *ALT* alanine aminotransferase, *AST* aspartate aminotransferase, *ILD* interstitial lung disease

5 Conclusions

In conclusion, in our retrospective analysis, prophylactic oral minocycline treatment significantly reduced the incidence of acneiform rash and xerosis, but not that of paronychia, induced by erlotinib during erlotinib plus gemcitabine treatment in patients with advanced pancreatic cancer. This finding should be confirmed in future randomized controlled studies. Prophylactic minocycline treatment appears to be useful for the management of erlotinib-related acneiform rash and xerosis during treatment with erlotinib plus gemcitabine in patients with advanced pancreatic cancer.

Acknowledgments This manuscript was prepared without the help of any funding source. A. Shinohara, M. Ikeda, H. Okuyama, M. Kobayashi, H. Funazaki, S. Mitsunaga, S. Shimizu, I. Ohno, H. Takahashi, Y. Ichida, K. Takahashi, T. Okusaka and S. Saitoh have no conflicts of interests to declare.

References

1. Moore MJ, Goldstein D, Hamm J, Figer A, et al. Erlotinib plus gemcitabine compared with gemcitabine alone in patients with advanced pancreatic cancer: a phase III trial of the national cancer institute of canada clinical trial group. J Clin Oncol. 2007;25:1960–6.
2. Okusaka T, Furuse J, Funakoshi A, et al. Phase II study of erlotinib plus gemcitabine in Japanese patients with unresectable pancreatic cancer. Cancer Sci. 2011;102:425–31.
3. Nakagawa K, Kudoh S, Ohe Y, et al. Postmarketing surveillance study of erlotinib in Japanese patients with non-small-cell lung cancer (NSCLC): an interim analysis of 3488 patients (POLARSTAR). J Thorac Oncol. 2012;7:1296–303.
4. Galimont-Collen AF, Vos LE, Lavrijsen AP, et al. Classification and management of skin, hair, nail and mucosal side-effects of epidermal growth factor receptor (EGFR) inhibitors. Eur J Cancer. 2007;43:845–51.
5. Scope A, Agero AL, Dusza SW, et al. Randomized double-blind trial of prophylactic oral minocycline and topical tazarotene for cetuximab-associated acne-like eruption. J Clin Oncol. 2007;25:5390–6.
6. Lacouture ME, Michell EP, Piperdi B, et al. Skin toxicity evaluation protocol with panitumumab (STEPP), a phase II, open-label, randomized trial evaluating the impact of a pre-emptive skin treatment regimen on skin toxicities and quality of life in patients with metastatic colorectal cancer. J Clin Oncol. 2010;28:1351–7.
7. Wacker B, Nagrani T, Weinberg J, et al. Correlation between development of rash and efficacy in patients treated with the epidermal growth factor receptor tyrosine kinase inhibitor erlotinib in two large phase III studies. Clin Cancer Res. 2007;13:3913–21.
8. Wheatley-Price P, Ding K, Seymour L, et al. Erlotinib for advanced non-small-cell lung cancer in the elderly: an analysis of

the National Cancer Institute of Canada Clinical Trials Group study BR.21. J Clin Oncol. 2008;26:2350–7.
9. Jatoi A, Green EM, Rowland KM, et al. Clinical predictors of severe cetuximab-induced rash: observation from 933 patients enrolled in North Central Cancer Treatment Group study N0147. Oncology. 2009;77:120–3.
10. Perez-Soler R, Chachoua A, Hammond LA, et al. Determinations of tumor response and survival with erlotinib in patients with non-small-cell lung cancer. J Clin Oncol. 2004;22:3238–47.
11. Soulieres D, Senzer NN, Vokes EE, et al. Multicenter phase II study of erlotinib, an oral epidermal growth factor receptor tyrosine kinase inhibitor, in patients with recurrent or metastatic squamous cell cancer of the head and neck. J Clin Oncol. 2004;22:3238–47.
12. Nanney LB, Stoscheck CM, King LE Jr, et al. Immunolocalization of epidermal growth factor receptors in normal developing human skin. J Invest Dermatol. 1990;94:742–8.
13. Li T, Perez-Soler R. Skin toxicities associated with epidermal growth factor receptor inhibitors. Targ Oncol. 2009;4:107–19.
14. Pastore S, Mascia F, Mariotti F, et al. ERK1/2 regulates epidermal chemokine expression and skin inflammation. J Immunol. 2005;174:5047–56.
15. Lacouture ME. Mechanisms of cutaneous toxicities to EGFR inhibitors. Nat Rev Cancer. 2006;6:803–12.
16. Pruzanski W, Greenwald RA, Street IP, et al. Inhibition of enzymatic activity of phospholipases A2 by minocycline and doxycycline. Biochem Pharmacol. 1992;44:1165–70.
17. Amin AR, Attur MG, Thakker GD, et al. A novel mechanism of action of tetracyclines: effects on nitric oxide synthases. Proc Natl Acad Sci. 1996;93:14014–9.
18. Dreno B, Bettoli V, Ochsendorf F, et al. European recommendations on the use of oral antibiotics for acne. Eur J Dermatol. 2004;14:391–9.
19. Vincent JA, Mohr S. Inhibition of caspase-1/interleukin-1beta signaling prevents degeneration of retinal capillaries in diabetes and galactosemia. Diabetes. 2007;56:224–30.
20. Shu KY, Kindler HL, Medenica M, et al. Doxycycline for the treatment of paronychia induced by the epidermal growth factor receptor inhibitor cetuximab. Br J Dermatol. 2006;154:191–2.
21. Stintzing S, Kapaun C, Laubender RP, et al. Prognostic value of cetuximab-related skin toxicity in metastatic colorectal cancer patients and its correlation with parameters of the epidermal growth factor receptor signal transduction pathway: results from a randomized trial of the GERMAN AIO CRC Study Group. Int J Cancer. 2013;132:236–45.
22. Migliaccio A, Castoria G, Di Domenico M, et al. Steroid-induced androgen receptor-oestradiol receptor-Src complex triggers prostate cancer cell proliferation. EMBO J. 2000;19:5406–17.
23. Migliaccio A, Castoria G, Di Domenico M, et al. Crosstalk between EGFR and extranuclear steroid receptors. Ann NY Acad Sci. 2006;1089:194–200.

OPEN

Therapeutic Priority of the PI3K/AKT/mTOR Pathway in Small Cell Lung Cancers as Revealed by a Comprehensive Genomic Analysis

Shigeki Umemura, MD, PhD, Sachiyo Mimaki, MS, † Hideki Makinoshima, PhD, † Satoshi Tada, MS, † Genichiro Ishii, MD, PhD,‡ Hironobu Ohmatsu, MD,* Seiji Niho, MD, PhD,* Kiyotaka Yoh, MD,*,† Shingo Matsumoto, MD, PhD,*,† Akiko Takahashi, MD,* Masahiro Morise, MD, PhD,* Yuka Nakamura, BS,‡ Atsushi Ochiai, MD, PhD,‡ Kanji Nagai, MD, PhD,§ Reika Iwakawa, PhD,‖ Takashi Kohno, PhD,‖ Jun Yokota, MD, PhD,‖ Yuichiro Ohe, MD, PhD,* Hiroyasu Esumi, MD, PhD,† Katsuya Tsuchihara, MD, PhD,† and Koichi Goto, MD, PhD,**

Introduction: The information regarding therapeutically relevant genomic alterations in small cell lung cancer (SCLC) is not well developed. We analyzed the SCLC genome using an integrative approach to stratify the targetable alterations.

Methods: We performed whole exon sequencing (n = 51) and copy number analysis (n =47) on surgically resected tumors and matched normal tissue samples from treatment-naive Japanese SCLC patients.

Results: The demographics of the 51 patients included in this study were as follows: median age, 67 years (range, 42–86 years); female, 9 (18%); history of smoking, 50 (98%); and pathological stage I/II/III/IV, 28/13/9/1, respectively. The average number of nonsynonymous mutations was 209 (range, 41–639; standard deviation, 130). We repeatedly confirmed the high prevalence of inactivating mutations in *TP53* and *RB1*, and the amplification of *MYC* family members. In addition, genetic alterations in the PI3K/AKT/mTOR pathway were detected in 36% of the tumors: *PIK3CA*, 6%; *PTEN*, 4%; *AKT2*, 9%; *AKT3*, 4%; *RICTOR*, 9%; and *mTOR*, 4%. Furthermore, the individual changes in this pathway were mutually exclusive. Importantly, the SCLC cells harboring active *PIK3CA* mutations were potentially targetable with currently available PI3K inhibitors.

Conclusions: The PI3K/AKT/mTOR pathway is distinguishable in SCLC genomic alterations. Therefore, a sequencing-based comprehensive analysis could stratify SCLC patients by potential therapeutic targets.

Key Words: Lung cancer, Small cell, Genome, Comprehensive, PI3K/AKT/mTOR.

(*J Thorac Oncol.* 2014;9: 1324–1331)

Small cell lung cancer (SCLC) comprises approximately 15% of all lung cancers,[1] and it is an exceptionally aggressive malignancy with a high proliferative index and an unusually strong predilection for early metastasis.[2] Despite extensive basic and clinical research over the past 30 years, little progress has been made[2] in treating this disease.

A better understanding of the genomic changes in SCLC is essential to identify new therapeutic targets. Genomic analyses have revealed genetically altered therapeutic targets in lung adenocarcinoma[3–5] and squamous cell lung carcinoma.[6] However, a systematic genomic analysis of SCLC is difficult because this cancer subtype is rarely treated surgically, resulting in the lack of suitable tumor specimens for comprehensive analysis.

Two reports regarding the comprehensive genomic analysis of SCLC with a relatively small number of samples have been published recently. These reports suggested that transcriptional deregulation (i.e., via *RB1*, *SOX2*, *MYC* family members and chromatin modifiers) might play a role in SCLC biology.[7,8] However, to date, attempts to develop targeted therapies toward these transcriptional deregulations have had limited success.

Activating alterations to oncogenes, such as receptor tyrosine kinases (RTKs) and PI3K/AKT/mTOR pathway proteins,[9–13] are regarded as successful therapeutic targets. We conducted a comprehensive genomic study in over 50 SCLC cases, and we found a higher penetrance of activating alterations of the PI3K/AKT/mTOR pathway that act in a mutually exclusive manner.

*Division of Thoracic Oncology, National Cancer Center Hospital East; †Exploratory Oncology Research and Clinical Trial Center, National Cancer Center; ‡Pathology Division, Research Center for Innovative Oncology, National Cancer Center Hospital East; §Division of Thoracic Surgery, National Cancer Center Hospital East, Kashiwa, Japan; and ‖Division of Genome Biology, National Cancer Center Research Institute, Chuo-ku, Tokyo, Japan.

This work was partly presented at the Annual Meeting of the American Society of Clinical Oncology, May 31–June 4, 2013, Chicago, IL. This study was performed as a research program of the Project for Development of Innovative Research on Cancer Therapeutics (P-Direct), Ministry of Education, Culture, Sports, Science and Technology of Japan, and it was supported by JSPS KAKENHI Grant Number 24300346, 26870876 and National Cancer Center Research and Development Fund (23-A-8, 15).

Disclosures: The authors declare no conflicts of interest.

Address for correspondence: Katsuya Tsuchihara, MD, PhD, Exploratory Oncology Research and Clinical Trial Center, National Cancer Center, 6-5-1 Kashiwanoha, Kashiwa 277-8577, Japan. E-mail: ktsuchih@east.ncc.go.jp

ISSN: 1556-0864/14/0909-1324

PATIENTS AND METHODS

Samples

This study was approved by the Institutional Review Board (IRB) of the National Cancer Center, Japan (IRB number: 2011-201). All data used in this study were obtained from a database at the Division of Thoracic Oncology, National Cancer Center Hospital East, Kashiwa, Japan.

From July 1992 to March 2012, we consecutively collected 1042 SCLC cases at our hospital. Fifty-five of these cases were included in the current study based on the following criteria: a surgical resection or mediastinoscopy was performed; a re-review confirmed a pathological diagnosis of SCLC; the tumor specimens contained a minimum of 70% tumor cells; enough tissue was obtained for a comprehensive analysis; the patient did not receive any neoadjuvant treatment; and the corresponding normal tissue, which was obtained from paraffin-embedded blocks of resected lung tissue that was microscopically free of cancer cells, was also available for analysis. We analyzed the exomes of these 55 samples to assess their mutational burden.

Depending on the tissue size, three to six sections (10 μm thickness) were cut. For the tumors showing a combined SCLC and other histology, only the SCLC compartment was dissected and used for analysis. Total DNA was obtained from formalin- ($n = 43$) or methanol-fixed ($n = 12$) paraffin-embedded tumors and matched normal tissue samples. All patients (100%) were Japanese.

Among these 55 cases, four exome data sets did not meet the sequence quality requirement and were excluded from further analyses. In addition, 48 samples received copy number analysis using single nucleotide polymorphism array data.

Procedures

The detailed experimental procedures are described in the Supplemental Information section (Supplemental Digital Content 1, http://links.lww.com/JTO/A625)

Whole Exon Sequencing and Copy Number Analysis

The Absolutely RNA FFPE kit (modified protocol for DNA extraction, Agilent Technologies, Santa Clara, CA) was used to prepare the DNA. Using 1 μg of dsDNA, quantified by Quant-iT PicoGreen dsDNA Reagent and Kits (Life Technologies, Carlsbad, CA), the exome-sequencing libraries were prepared. All exomes were captured using the SureSelect Human All Exon V4+UTRs Kit (Agilent Technologies) (71 mb). The exome capture libraries were sequenced by HiSeq 2000 (Illumina, San Diego, CA) to generate 100-bp paired-end data.

The Illumina HumanOmniExpress-FFPE BeadChip assay was used to analyze the genotype, DNA copy number, and loss of heterozygosity (LOH) in 48 primary-normal paired samples. All samples, except for 1 ($n = 47$), passed our quality control metrics for sample identity and data quality. A subset of 693,000 high-quality single nucleotide polymorphisms was selected for all analyses (Supplemental Figure 1, Supplemental Digital Content 2, http://links.lww.com/JTO/A626). A gene was considered copy number amplified if the calculated copy number in a sample was more than or equal to 4, and a gene was considered copy loss if the copy number in a sample was 0. Recurrent genomic regions with DNA copy gain and loss were identified using GISTIC, version 2.0.[14,15]

Identification of Significantly Mutated Genes

Significantly mutated genes were identified according to a previously reported protocol.[16] The length of the total coding sequence regions was represented as N (approximately 39.8 mb). When a patient (patient i) harbored a total of m_i single nucleotide variants (SNVs), the probability that the patient harbored SNVs in gene t (length: n) was calculated as follows:

$$P_{t,i} = 1-(1-\mathrm{m_i}/\mathrm{N})^{\mathrm{n}(t)}$$

The sum of $P_{t,i}$ in 51 samples was represented as the expected number of cases with SNVs in gene t:

$$\mathrm{P}_t = \sum_{i=1}^{51}(1-(1-\mathrm{m_i}/\mathrm{N})^{\mathrm{n}(t)})$$

The p values of the observed number were calculated using the binomial probability function with R pbinom.

Cancer Census Genes and Analysis of Hot Spot Mutations

We defined the cancer census genes as follows: 487 genes listed in the Catalogue of Somatic Mutations in Cancer (COSMIC) database (release version 64; http://cancer.sanger.ac.uk/cancergenome/progects/cosmic/) and 13 genes reported by Peifer et al.[7] were considered candidate driver genes. To analyze hot spot mutations, mutation data from the SCLC cases were downloaded from the COSMIC database (release version 64 or 68).

Cell Lines and Assays

The cell lines were cultured in RPMI-1640 supplemented with 10% fetal bovine serum (FBS) or hydrocortisone, insulin, transferrin, estradiol, and selenium (HITES) medium with 5% FBS. Then, 10,000 cells were plated in three replicates into 96-well plates. After 72 hours incubation with inhibitors, cell viability was analyzed with a WST-8 assay and a Cell Counting Kit-8 (Dojindo, Kumamoto, Japan). Western blotting was performed as described in the Supplemental Information section (Supplemental Digital Content 1, http://links.lww.com/JTO/A625).

RESULTS

Patient Characteristics

The characteristics of the available patient exome data ($n = 51$) are summarized in Table 1 and Supplemental Table 3 (Supplemental Digital Content 3, http://links.lww.com/JTO/A627). Fifty patients received surgical resections and one patient received a mediastinoscopy. Forty-two patients were male and nine were female. The median age at the time of surgical resection was 67 years (range, 42–86 years). Of the 51 patients, 50 (98%) had a history of smoking, and the pathological stages were distributed as follows: stage I, 28 patients; stage II, 13

TABLE 1. Patient Characteristics

Characteristic	No. of Patients
Total	51
Gender	
Male/female	42/9
Age, years	
Median (range)	67 (42–86)
Performance status	
0/1/2	35/15/1
Smoking status	
Never/ever	1/50
Pack years	
Median (range)	47 (0–98)
Histology	
Pure SCLC/combined SCLC	40/11
Pathological stage	
I/II/III/IV	28/13/9/1
Vascular invasion	
Absent/present	8/43
Lymphatic invasion	
Absent/present/unknown	31/19/1
Pleural invasion	
Absent/present/unknown	31/19/1
Tumor diameter	
Median (range)	2.5 (1.1–13.0)

patients; stage III, nine patients; and stage IV, one patient. All patients were positive for at least one of the following neuroendocrine markers: CD56, chromogranin A, or synaptophysin.

Somatic Point Mutations

The exome capture, sequencing, and analysis of the 51 SCLC tumor–normal tissue pairs identified 10,640 protein-altering somatic mutations, including 9376 missense, 707 nonsense, and 557 protein-altering insertions and/or deletions (INDEL) (Supplemental Table 4, Supplemental Digital Content 3, http://links.lww.com/JTO/A627). The SCLC tumors had an average of 209 protein-altering SNVs (range 41–639) per case, with a mean nonsynonymous mutation rate of 6.15 mutations per mega-base (Supplemental Figure 2, Supplemental Digital Content 2, http://links.lww.com/JTO/A626). Significantly mutated genes are determined as Supplemental Table 5 (Supplemental Digital Content 3, http://links.lww.com/JTO/A627). Overall, 414 genes had a p value of less than 0.01 and 1321 genes had a p value of less than 0.05.

A description of the significantly mutated cancer census genes (p value <0.05 in our data set) is provided in Table 2. Notably, *TP53* was the most frequently mutated gene (mutation frequency of 80%, p value of 5.81E–69). The mutation frequencies and p values of cancer census genes were 39% and 6.42E–22, 16% and 0.00019, 10% and 0.0017 for *RB1*, *ROS1*, and *RET*, respectively. Mutations of histone modifiers were also recurrently identified in this study; *CREBBP* was mutated in 6% of the patients, and *EP300* was mutated in 4% of the patients (Fig. 1). Recently reported candidate driver genes were also recurrently identified in the PI3K/AKT/mTOR signaling pathway. Three patients (6%) had mutations in *PIK3CA* (one E545K, two others), and two patients (4%) had mutations in the *PTEN* C2 domain (Supplemental Figure 3, Supplemental Digital Content 2, http://links.lww.com/JTO/A626).

To validate the whole exon sequencing data, we performed Sanger sequencing for the variants including four SNVs of *PIK3CA* and *ROS1* and a deletion of *KIT* in five individual tumor samples. All the variants detected using whole exon sequencing were reproduced using conventional Sanger sequencing (Supplemental Figure 4, Supplemental Digital Content 2, http://links.lww.com/JTO/A626). Furthermore, we designed a custom target-capturing panel containing all the coding exons of 244 genes. Four tumor samples were applied to the target resequencing, and all 41 SNVs or indels in these tumor genomes were reproducibly identified (Supplemental Table 6, Supplemental Digital Content 3, http://links.lww.com/JTO/A627).

Copy Number Analysis

Next, we applied a novel algorithm to identify the significant somatic copy number alterations (Supplemental Figure 5, Supplemental Digital Content 2, http://links.lww.com/JTO/A626). A description of frequently amplified cancer census genes (GISTIC $-\log_{10}$ q score ≥ 1.50) is provided in Table 3. *MYC* family members were frequently amplified (GISTIC q scores were 2.50, 1.65, and 1.57 for *MYCL1*, *MYCN*, and *MYC*, respectively). The amplifications affected *MYCL1* (4/47 cases), *MYC* (1/47 cases), and *MYCN* (1/47 cases). All *MYC* family member amplifications (13% of cases) were mutually exclusive (Fig. 1). In addition, gene amplifications were frequently found in the PI3K/AKT/mTOR signaling pathway (GISTIC q scores were 2.45 and 1.22 for *AKT2* and *RICTOR*, respectively). The gene amplifications in PI3K/AKT/mTOR signaling were observed in *AKT2* (4/47 cases) and *RICTOR* (3/47 cases), and they were also mutually exclusive (Fig. 1). Previously reported amplifications involving *SOX2* (1/47 cases) and *KIT* (1/47 cases) were also identified.

Recurrent Mutations at the Same Position

Forty genes with recurrent somatic mutations at the same position were identified in this study and the COSMIC database (Table 4). *TP53*, the well-characterized tumor suppressor gene, had 29 different positions that mutated more than or equal to two times (total recurrent samples, 134). *RB1* had four different positions that mutated two or three times. The remaining 38 genes had one position that mutated two or three times. Well-established activating mutations in *PIK3CA*, the catalytic subunit of phosphoinositide-3 kinase (E545), were also detected in another SCLC cohort.

PI3K/AKT/mTOR Pathway Alteration

Because of the large number of somatic point mutations and focal amplifications found in the PI3K/AKT/mTOR signaling pathway (e.g., *PIK3CA*, *PTEN*, *AKT2*, and *RICTOR*), we focused our investigation on the changes in the PI3K/AKT/mTOR pathway. We observed that the PI3K/AKT/mTOR pathway was altered in 17/47 (36%) of the SCLC tumors (Fig. 1), and all altered genes in the PI3K/AKT/mTOR pathway were mutually exclusive. There was no difference in the

TABLE 2. Significantly Mutated Cancer Census Genes (*$p < 0.05$ in This Study)

	This Data Set ($n = 51$)			COSMIC Database	
Symbol	Mutated Case	Mutation Frequency (%)	p Value*	Mutated Case/Total	Mutation Frequency (%)
TP53	41	80	5.81E–69	235/308	76
RB1	20	39	6.42E–22	99/181	55
ROS1	8	16	0.00019	7/65	11
RET	5	10	0.0017	4/147	3
IKZF1	4	8	0.0017	0/57	0
CD79B	2	4	0.0042	0/61	0
PAX7	3	6	0.0074	3/63	5
HIP1	4	8	0.0076	1/62	2
CDH11	4	8	0.0086	0/62	0
MN1	4	8	0.014	1/61	2
PTEN	2	4	0.017	39/309	13
ERBB2	4	8	0.018	1/167	1
LPP	3	6	0.019	0/62	0
MLL2	6	12	0.021	7/57	12
BCL11B	3	6	0.022	0/63	0
LMO1	1	2	0.023	0/62	0
NR4A3	3	6	0.028	1/56	2
ZNF521	4	8	0.031	10/62	16
PIK3CA	3	6	0.034	38/272	14
WT1	2	4	0.040	1/127	1
TRIM33	3	6	0.041	1/62	2
PBRM1	4	8	0.042	1/61	2
FUS	2	4	0.043	0/62	0
ABL1	3	6	0.044	2/63	3
RPN1	2	4	0.045	0/57	0
BTG1	1	2	0.045	0/62	0

*p value., P binom.

clinical characteristics, such as smoking status, gender, and age, between the PI3K/AKT/mTOR pathway-affected group (Group A) and the PI3K/AKT/mTOR pathway-unaffected group (Group B). The frequencies of *TP53* and *RB1* mutations were identical between Group A and Group B. However, more *MYC* family genes tended to be amplified in Group B; Group A did not harbor *KRAS* or *BRAF* mutations, and most patients in Group A did not have MAPK/ERK pathway changes.

The correlation between the PI3K/AKT/mTOR pathway changes and RTKs is shown in Supplemental Figure 6 (Supplemental Digital Content 2, http://links.lww.com/JTO/A626). The changes in various targetable RTK genes were detected, such as *ERBB2* ($n = 4$), *KIT* ($n = 2$), *PDGFRA* ($n = 3$), *PDGFRB* ($n = 2$), *KDR* ($n = 3$), *MET* ($n = 1$), *ROS1* ($n = 8$), and *RET* ($n = 5$). However, none of these genes showed a recurrent mutation at the same point in this data set or the COSMIC database. The PI3K/AKT/mTOR pathway status did not correlate with the RTK changes.

Drug Sensitivity

To further investigate whether the PI3K/AKT/mTOR pathway could be a feasible therapeutic target in SCLC, we tested the in vitro drug sensitivity of the SCLC cell lines using the clinically developed compounds targeting this pathway (Fig. 2 and Supplemental Figure 7, Supplemental Digital Content 2, http://links.lww.com/JTO/A626). We selected three SCLC cell lines with genetic alterations in the PI3K/AKT/mTOR pathway: H446 (*PTEN*-loss, *MYC*-amplified), H1048 (*PIK3CA* mutation), and H1694 (*AKT3*-amplified). We also examined H82 (*MYC*-amplified) and H209, which do not display activation of the PI3K/AKT/mTOR pathway. Using these cell lines, we assessed the efficacy of four compounds that inhibit the PI3K/AKT/mTOR pathway and are in on-going phase I/II trials: BEZ235 (PI3K and mTOR inhibitor), BKM120 (PI3K inhibitor), INK128 (mTOR inhibitor), and MK2206 (AKT inhibitor), as well as one cytotoxic agent, cisplatin. None of the cell lines showed apparent cytotoxicity in response to doses up to 1 μM cisplatin. Conversely, all PI3K/AKT/mTOR inhibitors significantly impaired the proliferation of the SCLC cell lines. H1048, which harbors a *PIK3CA* mutation (H1047R), was the most sensitive to all of the PI3K/AKT/mTOR inhibitors, with IC50 values of 3.8, 5.4, 99.9, and 195.4 nM for INK128, BEZ235, MK2206, and BKM120, respectively. BEZ235 was the most effective compound to specifically inhibit H1048 cell growth

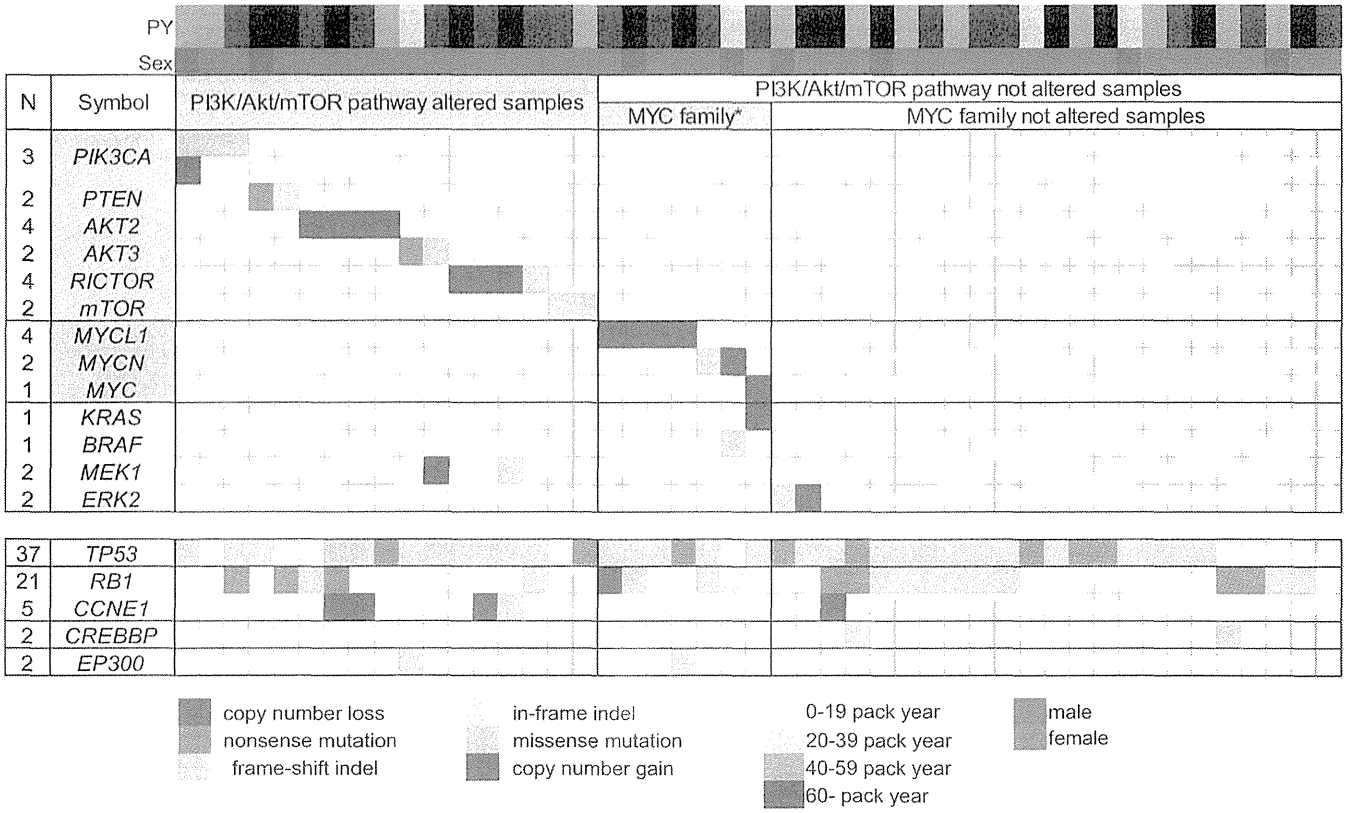

FIGURE 1. An overview of the key driver mutations and major associated clinical features of 47 SCLC samples. The number of events per gene is noted on the left. The genes are displayed as rows, and the samples are displayed as columns, with major associated clinical features.
PY, PACK YEARS; MYC FAMILY*, MYC FAMILY ALTERED SAMPLES.

TABLE 3. Frequently Mutated Cancer Census Genes ($-\log_{10}$ q score ≥1.5)

	This Data Set (n = 47)
Symbol	**$-\log_{10}$ (q score)**
MYB	3.40
MYCL1	2.50
AKT2	2.45
CLTCL1	2.34
LIFR	2.21
IL7R	2.13
THRAP3	2.09
ETV5	2.05
BCL6	1.99
EIF4A2	1.93
LPP	1.89
PAX5	1.89
ZNF384	1.86
ARID1A	1.65
MYCN	1.65
FANCG	1.65
MYC	1.57
MDS2	1.52

(IC50 = 5.4), with an IC50 value greater than 10-fold lower than that of H82 (IC50 = 58.3 nM) and fivefold lower than that of H209 (IC50 = 29.7 nM). In contrast, H446 (IC50 = 33.3 nM) and H1694 cells (IC50 = 52.5 nM) were relatively resistant to BEZ235 treatment.

The impact of BEZ235 on AKT phosphorylation in SCLC cells was investigated using Western blot analysis. AKT was activated in the H446 and H1048 cells under these culture conditions, and it was effectively inhibited after being treated with 10 nM BEZ235. Conversely, constitutive phosphorylation of AKT was not observed in H1694 cells, even when pan-AKT was over-expressed. In addition, AKT phosphorylation was not detected in the H82 and H209 cells. Regarding factors located downstream of mTOR, S6RP was phosphorylated in all five SCLC cell lines. Especially, the phosphorylation level was high in AKT-activated H446 and H1048 cells. BEZ235 significantly reduced the phosphorylation of S6RP in all the cells.

To evaluate the contribution of PI3K/AKT/mTOR signaling to SCLC cell proliferation, we used RNA interference (RNAi) to down-regulate the expression of *PIK3CA* in H1048 cells. The transient silencing of *PIK3CA* impaired the phosphorylation of AKT and S6RP (Supplemental Figure 8, Supplemental Digital Content 2, http://links.lww.com/JTO/A626). In addition, *PIK3CA* silencing induced a decrease in the proliferation of H1048 cells.

TABLE 4. The Recurrent Mutations Detected at the Same Position in This Study and the COSMIC Database

Gene	Recurrent in This Study (no.)	No. in This Data Set	Recurrent in COSMIC Database (no.)	No. in COSMIC Database	Total
TP53	Q38 (1) T155 (1) V157 (1) R158 (2) A159 (1) M160 (1) A161 (1) Y163 (2) R175 (1) C176 (2) H179 (1) Q192 (1) D208 (1) R209 (1) R213 (1) S215 (2) Y220 (1) R248 (1) R249 (2) L265 (1) G266 (2) R273 (1) R283 (2) E286 (1) E294 (1) E298 (1) Q317 (1) R337 (2) R342 (1)	37	Q38 (1) T155 (4) V157 (11) R158 (3) A159 (1) M160 (1) A161 (1) Y163 (2) R175 (4) C176 (2) H179 (7) Q192 (2) D208 (1) R209 (2) R213 (3) S215 (1) Y220 (8) R248 (7) R249 (11) L265 (1) G266 (3) R273 (8) R283 (1) E286 (5) E294 (3) E298 (2) Q317 (1) R342 (1)	97	134
RB1	T543 (2) W78 (1) W195 (1) E322 (1)	5	W78 (1) W195 (2) E322 (1)	4	9
ABRA	S276 (2)	2		0	2
AP3M2	T72 (2)	2		0	2
CLEC4G	R23 (2)	2		0	2
DACT1	V481 (2)	2		0	2
DPP6	Q345 (2)	2		0	2
DUSP27	D886 (2)	2		0	2
GPR149	R540 (2)	2		0	2
KIAA2022	Q738 (2)	2		0	2
OR9G1	C168 (2)	2		0	2
PCDHGA5	E782 (2)	2		0	2
PDE4C	P39 (2)	2		0	2
PJA1	E182 (2)	2		0	2
ZFP1	Q287 (2)	2		0	2
B2M	M1 (1)	1	M1 (2)	2	3
PIK3CA	E545 (1)	1	E545 (2)	2	3
AFF2	D506 (1)	1	D506 (1)	1	2
ASTN1	R184 (1)	1	R184 (1)	1	2
BEND3	G263 (1)	1	G263 (1)	1	2
C8A	R438 (1)	1	R438 (1)	1	2
CREB3L3	P82 (1)	1	P82 (1)	1	2
CST4	R46 (1)	1	R46 (1)	1	2
DEFB112	R112 (1)	1	R112 (1)	1	2
GPR139	T322 (1)	1	T322 (1)	1	2
HCN1	Q772 (1)	1	Q772 (1)	1	2
ITGA4	R481 (1)	1	R481 (1)	1	2
JAM3	Y31 (1)	1	Y31 (1)	1	2
KCNJ12	R261 (1)	1	R261 (1)	1	2
LIFR	Q978 (1)	1	Q978 (1)	1	2
LRRC52	A258 (1)	1	A258 (1)	1	2
MED23	N1095 (1)	1	N1095 (1)	1	2
MUC6	P27 (1)	1	P27 (1)	1	2
OPN4	C303 (1)	1	C303 (1)	1	2
OR10S1	A283 (1)	1	A283 (1)	1	2
OR2W1	I206 (1)	1	I206 (1)	1	2
OR5F1	S265 (1)	1	S265 (1)	1	2
OR5L1	S267 (1)	1	S267 (1)	1	2
SLC28A3	Q261 (1)	1	Q261 (1)	1	2
ZNF382	C278 (1)	1	C278 (1)	1	2

no., number Recurrent (no.), positions with recurrent mutations (no. of instances).

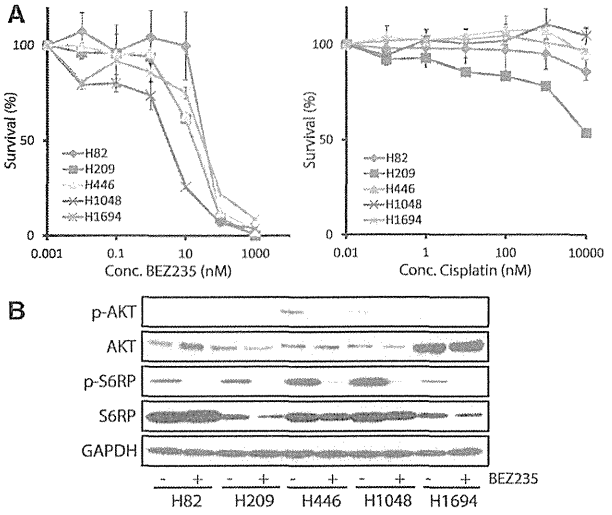

FIGURE 2. (*A*) The concentration–response cell survival curves of SCLC cell lines with or without genetic alteration in the PI3K/AKT/mTOR pathway in response to BEZ235 (nM) and Cisplatin (nM). The *PIK3CA* mutation positive cell line, H1048, is relatively sensitive to BEZ235. The H82 and H209 cell lines are negative controls. (*B*) Western blotting was used to investigate the impact of BEZ235 on AKT phosphorylation and S6RP phosphorylation in the SCLC cells. AKT was activated in H446 and H1048 cells, and it was inhibited after being treated with 10 nM BEZ235. AKT was amplified but not constitutively phosphorylated in the H1694 cells. AKT phosphorylation was not detected in the negative control cell lines, H82 and H209. With regard to factors located downstream of mTOR, S6RP was phosphorylated in all five SCLC cell lines. Especially, the phosphorylation level was high in AKT-activated H446 and H1048 cells. BEZ235 significantly reduced the phosphorylation of S6RP in all the cells.

DISCUSSION

We performed an integrative genomic analysis of SCLC in Japanese patients. The SCLC tumors had a significantly high mutation rate. An analysis of the base-level transitions and transversions showed that G-to-T transversions were predominant (Supplemental Figure 2, Supplemental Digital Content 2, http://links.lww.com/JTO/A626), which was consistent with the demonstrated effects of tobacco smoke carcinogens on DNA.[8,17] A high prevalence of inactivating mutations in *TP53* and *RB1* and recently reported candidate driver genes, including the mutations of histone modifiers (*CREBBP*[7] and *EP300*[7]), were recurrently observed along with the amplification of *MYC* family members.[7,14,18,19] These data indicate that the genomic landscape of SCLC is equivalent between Asian and Caucasian populations.[7,8,17,18]

SCLC is characterized by aggressive growth and a poor prognosis, and no single molecular targeted drug has shown any clinical efficacy over an extended period. A number of inhibitors targeting changes in RTKs are currently used in clinical use. Alterations in well-known, targetable RTK genes, such as *ERBB2*, *KIT*, *PDGFRA*, *PDGFRB*, *KDR*, *MET*, *ROS1*, and *RET*, were detected in this study. However, these alterations did not overlap with previously reported activating mutations.

The PI3K/AKT/mTOR signaling pathway is involved in the survival, proliferation, and migration of SCLC cell lines.[13] We confirmed the activation of the PI3K pathway in the SCLC-derived cell lines. AKT protein overexpression was observed in the *AKT3*-amplified H1694 cells, and phosphorylated-AKT and S6RP were increased in the *PTEN*-lacking H446 cells and *PIK3CA*-mutated H1048 cells. In addition, the significant decrease in the proliferation of H1048 cells induced by *PIK3CA* silencing suggested that the proliferation of these cells was strongly dependent on the PI3K/AKT/mTOR pathway (Supplemental Figure 8, Supplemental Digital Content 2, http://links.lww.com/JTO/A626). Consistently, genetic changes in the PI3K/AKT/mTOR pathway were detected in approximately 40% of our clinical samples. In addition to high penetrance, these alterations occurred in a mutually exclusive manner. A similar trend was observed in another Japanese cohort of primary SCLC (Supplemental Table 7, Supplemental Digital Content 3, http://links.lww.com/JTO/A627). In addition to SCLC, a significant exclusion pattern among PI3K pathway molecules was observed in the systematic analysis of breast cancer genomes.[20] Together, these data suggest indispensable roles for this pathway in tumorigenesis.

Two specific inhibitors of mTORC1, everolimus[10] and temsirolimus,[11] were tested against SCLC in a Phase II study. However, single-agent antitumor activity was limited in unselected patients; the response rate in these studies was less than 10%. To improve the response to these inhibitors, the addition of PI3K inhibition has been suggested. The dual inhibition of PI3K and mTOR might be advantageous over single inhibition by suppressing a S6K feedback loop that leads to the pathway reactivation.[21] Based on this idea, an on-going phase I study of the PI3K and mTORC1/2 dual inhibitor, BEZ235, was designed for the patients with advanced solid tumors harboring *PIK3CA* or *PTEN* alteration (NCT01195376). In this study, we showed that the survival of the cisplatin-resistant SCLC cell lines was well suppressed by BEZ235, accompanied by the suppression of S6RP phosphorylation. Notably, the effect was most significant against H1048 cells, which harbor a *PIK3CA*-activating mutation.

However, we found that not all SCLC cell lines harboring PI3K/AKT/mTOR pathway alterations exhibited a similar sensitivity to BEZ235. Although AKT phosphorylation was significantly inhibited by BEZ235 in both the H446 cells and H1048 cells, the sensitivity of the H446 cells was less than that of the H1048 cells. *MYC* gene amplification reportedly evades PI3K-targeted therapy.[22] *MYC* amplification was demonstrated in H446 cells,[23,24] and this co-alteration could be one cause of the observed low sensitivity. Thus, to determine the most beneficial concentrations for patients, both direct target molecules and other interfering signaling pathways should be simultaneously assessed. In this study, no surgically resected tumors harbored co-alterations of the PI3K/AKT/mTOR pathway and MYC gene amplification. However, the sample size of this study and other published systemic analyses remained small, and many of the samples were obtained from relatively early-stage tumors. We should expand the sample size and further analyze samples of advanced tumors using biopsy, necropsy, and autopsy specimens to clarify the coexistence of oncogenic alterations in SCLC.

Although further large-scale validation studies are needed, our data suggest that evaluating the genetic status of molecules that modify the PI3K/AKT/mTOR signaling pathway, such as MYC family and MAPK pathway molecules, is essential to select patients with potential sensitivity to PI3K/AKT/mTOR inhibitors. In other words, enriching the study population by performing the integrative genomic analysis is essential when performing phase studies of PI3K/AKT/mTOR inhibitors in SCLC.

In conclusion, the SCLC genome possesses distinguishable genetic features in the PI3K/AKT/mTOR pathway. Genetic alterations in the PI3K/AKT/mTOR pathway were noted as a top therapeutic priority in SCLC. In addition to surgically resected samples, advanced tumors should be examined for comprehensive genomic analysis.

ACKNOWLEDGMENTS

This study was performed as a research program of the Project for Development of Innovative Research on Cancer Therapeutics (P-Direct), Ministry of Education, Culture, Sports, Science and Technology of Japan, and it was supported by JSPS KAKENHI Grant Number 24300346 and National Cancer Center Research and Development Fund (23-A-8, 15). The authors thank Ms. Fumiko Koh, Drs. Masao Yamaguchi, Hideki Okada, Keiju Aokage, Tomoyuki Hishida, Junji Yoshida, Keisuke Kirita, Eri Sugiyama, Yoshitaka Zenke, Tatsuya Yoshida, Yuji Matsumoto, and Yuuki Matsumura for their support and comments.

REFERENCES

1. Siegel R, Naishadham D, Jemal A. Cancer statistics, 2012. *CA Cancer J Clin* 2012;62:10–29.
2. William WN Jr, Glisson BS. Novel strategies for the treatment of small-cell lung carcinoma. *Nat Rev Clin Oncol* 2011;8:611–619.
3. Govindan R, Ding L, Griffith M, et al. Genomic landscape of non-small cell lung cancer in smokers and never-smokers. *Cell* 2012;150:1121–1134.
4. Kohno T, Ichikawa H, Totoki Y, et al. KIF5B-RET fusions in lung adenocarcinoma. *Nat Med* 2012;18:375–377.
5. Lipson D, Capelletti M, Yelensky R, et al. Identification of new ALK and RET gene fusions from colorectal and lung cancer biopsies. *Nat Med* 2012;18:382–384.
6. Cancer Genome Atlas Research Network. Comprehensive genomic characterisation of squamous cell lung cancers. *Nature* 2012; 489: 519–525.
7. Peifer M, Fernández-Cuesta L, Sos ML, et al. Integrative genome analyses identify key somatic driver mutations of small-cell lung cancer. *Nat Genet* 2012;44:1104–1110.
8. Rudin CM, Durinck S, Stawiski EW, et al. Comprehensive genomic analysis identifies SOX2 as a frequently amplified gene in small-cell lung cancer. *Nat Genet* 2012;44:1111–1116.
9. Pietanza MC, Ladanyi M. Bringing the genomic landscape of small-cell lung cancer into focus. *Nat Genet* 2012;44:1074–1075.
10. Tarhini A, Kotsakis A, Gooding W, et al. Phase II study of everolimus (RAD001) in previously treated small cell lung cancer. *Clin Cancer Res* 2010;16:5900–5907.
11. Pandya KJ, Dahlberg S, Hidalgo M, et al. A randomised, phase II trial of two dose levels of temsirolimus (CCI-779) in patients with extensive-stage small-cell lung cancer who have responding or stable disease after induction chemotherapy: a trial of the Eastern Cooperative Oncology Group (E1500). *J Thorac Oncol* 2007;2:1036–1041.
12. Voortman J, Lee JH, Killian JK, et al. Array comparative genomic hybridization-based characterization of genetic alterations in pulmonary neuroendocrine tumors. *Proc Natl Acad Sci U S A* 2010;107: 13040–13045.
13. Wojtalla A, Fischer B, Kotelevets N, et al. Targeting the phosphoinositide 3-kinase p110-α isoform impairs cell proliferation, survival, and tumor growth in small cell lung cancer. *Clin Cancer Res* 2013;19:96–105.
14. Mermel CH, Schumacher SE, Hill B, Meyerson ML, Beroukhim R, Getz G. GISTIC2.0 facilitates sensitive and confident localization of the targets of focal somatic copy-number alteration in human cancers. *Genome Biol* 2011;12:R41.
15. Beroukhim R, Getz G, Nghiemphu L, et al. Assessing the significance of chromosomal aberrations in cancer: methodology and application to glioma. *Proc Natl Acad Sci U S A* 2007;104:20007–20012.
16. Suzuki A, Mimaki S, Yamane Y, et al. Identification and characterization of cancer mutations in Japanese lung adenocarcinoma without sequencing of normal tissue counterparts. *PLoS One* 2013;8:e73484.
17. Pleasance ED, Stephens PJ, O'Meara S, et al. A small-cell lung cancer genome with complex signatures of tobacco exposure. *Nature* 2010;463:184–190.
18. Arriola E, Cañadas I, Arumí M, Rojo F, Rovira A, Albanell J. Genetic changes in small cell lung carcinoma. *Clin Transl Oncol* 2008;10:189–197.
19. Iwakawa R, Takenaka M, Kohno T, et al. Genome-wide identification of genes with amplification and/or fusion in small cell lung cancer. *Genes Chromosomes Cancer* 2013;52:802–816.
20. Cancer Genome Atlas Network. Comprehensive molecular portraits of human breast tumours. *Nature* 2012; 490: 61–70.
21. Gadgeel SM, Wozniak A. Preclinical rationale for PI3K/Akt/mTOR pathway inhibitors as therapy for epidermal growth factor receptor inhibitor-resistant non-small-cell lung cancer. *Clin Lung Cancer* 2013;14:322–332.
22. Ilic N, Utermark T, Widlund HR, Roberts TM. PI3K-targeted therapy can be evaded by gene amplification along the MYC-eukaryotic translation initiation factor 4E (eIF4E) axis. *Proc Natl Acad Sci U S A* 2011;108:E699–E708.
23. Brennan J, O'Connor T, Makuch RW, et al. myc family DNA amplification in 107 tumors and tumor cell lines from patients with small cell lung cancer treated with different combination chemotherapy regimens. *Cancer Res* 1991;51:1708–1712.
24. Sos ML, Dietlein F, Peifer M, et al. A framework for identification of actionable cancer genome dependencies in small cell lung cancer. *Proc Natl Acad Sci U S A* 2012;109:17034–17039.

European Journal of Radiology 83 (2014) e23–e35

Contents lists available at ScienceDirect

European Journal of Radiology

journal homepage: www.elsevier.com/locate/ejrad

Review

Primary staging of laryngeal and hypopharyngeal cancer: CT, MR imaging and dual-energy CT

Hirofumi Kuno[a,*], Hiroaki Onaya[b,1], Satoshi Fujii[c,2], Hiroya Ojiri[d,3], Katharina Otani[e,4], Mitsuo Satake[a,5]

[a] Diagnostic Radiology Division, National Cancer Center Hospital East, 6-5-1, Kashiwanoha, Kashiwa, Chiba 277-8577, Japan
[b] Diagnostic Radiology Division, National Cancer Center Hospital, 5-1-1 Tsukiji Chuo-ku, Tokyo 104-0045, Japan
[c] Pathology Division, Research Center for Innovative Oncology, National Cancer Center Hospital East, 6-5-1 Kashiwanoha, Kashiwa, Chiba 277-8577, Japan
[d] Department of Radiology, Jikei University School of Medicine, 3-25-18 Nishi-shinbashi Minato-ku, Tokyo 105-8461, Japan
[e] Imaging & Therapy Systems Division, Siemens Japan K.K., Gate City Osaki West Tower 1-11-1 Osaki, Shinagawa-ku, Tokyo 141-8644, Japan

ARTICLE INFO

Article history:
Received 12 April 2013
Received in revised form 23 July 2013
Accepted 20 October 2013

Keywords:
Laryngeal cancer
Hypopharyngeal cancer
Computed tomography
Magnetic resonance imaging
Dual-energy CT
Staging

ABSTRACT

Laryngeal and hypopharyngeal cancer, in particular T4a disease associated with cartilage invasion and extralaryngeal spread, needs to be evaluated accurately because treatment can impact heavily on a patient's quality of life. Reliable imaging tools are therefore indispensible. CT offers high spatial and temporal resolution and remains the preferred imaging modality. Although cartilage invasion can be diagnosed with acceptable accuracy by applying defined criteria for combinations of erosion, lysis and transmural extralaryngeal spread, iodine-enhanced tumors and non-ossified cartilage are sometimes difficult to distinguish. MR offers high contrast resolution for images without motion artifacts, although inflammatory changes in cartilage sometimes resemble cartilage invasion. With dual-energy CT, combined iodine overlay images and weighted average images can be used for evaluation of cartilage invasion, since iodine enhancement is evident in tumor tissue but not in cartilage. Extralaryngeal spread can be evaluated from CT, MR or dual-energy CT images and the routes of tumor spread into the extralaryngeal soft tissue must be considered; (1) via the thyrohyoid membrane along the superior laryngeal neurovascular bundle, (2) via the inferior pharyngeal constrictor muscle, and (3) via the cricothyroid membrane. Radiologists need to understand the advantages and limitations of each imaging modality for staging of laryngeal and hypopharyngeal cancer.

1. Introduction

Laryngeal and hypopharyngeal cancers are common malignant tumors in the head and neck, and most of such cases are squamous cell carcinomas [1]. In view of the functional and social importance of the larynx, any decision about the optimal management strategy for laryngeal or hypopharyngeal cancer must involve consideration of both potential survival and the functional consequences of any given treatment approach. Patients with T1, T2 and limited cartilage invasion disease can be considered positively for organ-preserving procedures such as radiation therapy alone, a combination of chemotherapy and radiation therapy, and function-preserving partial laryngectomy procedures [2–6]. Patients with T4a disease, particularly when the tumor extends through the cartilage into the soft tissue of the neck, often need aggressive treatments such as total laryngectomy [2,7,8], because the risks of recurrence and cartilage necrosis after radiotherapy alone are high [2–4]. Both CT and MR imaging are routinely used to differentiate between limited and gross cartilage invasion. However, cartilage invasion is sometimes overestimated, resulting in unnecessary total laryngectomies in some patients [9,10].

Currently, dual-energy CT is being investigated in several clinical fields [11–15], including the evaluation of head and neck cancer [16]. Since treatment is decided according to the precise extent and invasion pattern of a tumor, the findings of these imaging procedures play a crucial role in any multidisciplinary approach for management of laryngeal and hypopharyngeal cancer [17–19]. Rapid technological developments in recent years have made it necessary for all members of multidisciplinary teams to understand the

* Corresponding author. Tel.: +81 4 7133 1111x91311; fax: +81 4 7131 4724.
E-mail addresses: hkuno@east.ncc.go.jp (H. Kuno), honaya@ncc.go.jp (H. Onaya), sfujii@east.ncc.go.jp (S. Fujii), ojiri@jikei.ac.jp (H. Ojiri), katharina.otani@siemens.com (K. Otani), msatake@east.ncc.go.jp (M. Satake).
[1] Tel.: +81 3 3542 2511.
[2] Tel.: +81 4 7133 1111.
[3] Tel.: +81 3 3433 1111.
[4] Tel.: +81 3 3493 7429.
[5] Tel.: +81 4 7133 1111.

0720-048X/$ – see front matter © 2013 Elsevier Ireland Ltd. All rights reserved.
http://dx.doi.org/10.1016/j.ejrad.2013.10.022

Table 1
Primary tumor (T) staging according to the American Joint Committee on Cancer (AJCC) 7th edition (modified version by author).

	Laryngeal cancer			Hypopharyngeal cancer
	Supraglottic	Glottic	Subglottic	
T1	One subsite	(a) One vocal cord (b) both vocal cords	Limited to subglottis	≤2 cm and limited to one subsite
T2	More than one subsite	Extends to supra/sub glottis Impaired vocal cord mobility	Extends to glottis	>2–4 cm or more than one subsite
T3	PGS/PES or vocal cord fixation Inner cortex of thyroid cartilage Extends to postcricoid	PGS or vocal cord fixation Inner cortex of thyroid cartilage	Vocal cord fixation	>4 cm or vocal cord fixation
T4a	Tumor invades through the thyroid cartilage or extra-laryngeal spread		Tumor invades thyroid/cricoid cartilage or extra-laryngeal spread	
T4b	Tumor invades prevertebral space, encases carotid artery, or invades mediastinal structures			

Note: PGS = paraglottic space; PES = preepiglottic space.

potential applications, limitations, and appropriate criteria of these imaging modalities.

In this article, we review the significant role of imaging for staging of laryngeal and hypopharyngeal cancer. We discuss the appearances of T4a disease on conventional CT and MR images and illustrate how dual-energy CT can be applied for evaluation of laryngeal and hypopharyngeal cancer.

2. Primary tumor staging (T) of laryngeal and hypopharyngeal cancer

The system for staging of primary laryngeal (glottic, supraglottic and subglottic) and hypopharyngeal cancer is outlined in Table 1 (American Joint Committee on Cancer 2010) [20]. Clinical staging of the primary site is based on involvement of various subsites of the larynx or adjacent regions of the pharynx and vocal cord mobility. Assessment of the primary tumor is initially accomplished by clinical inspection, using indirect mirror and direct endoscopic examination with a fiberoptic nasolaryngoscope. However, these tumors have a tendency to spread submucosally, and this extension into deeply seated tissue planes can be easily missed by clinical examination alone [8,17,19]. Therefore, clinicians rely on imaging to predict which patients will have T3–4 disease. Even if the primary tumor has been clinically diagnosed as T1–2 disease on the basis of inspection, imaging is an important adjunct to exclude any T3–4 factor features or the presence of submucosal extension [8,21–23]. Therefore, cross-sectional imaging using CT or MR imaging is mandatory for completing the staging process, and should be included in the diagnostic workup.

For laryngeal cancer, the first imaging criterion that defines T3 lesions is extension into the paraglottic and/or preepiglottic space, irrespective of vocal cord mobility. In addition, tumor erosion limited to the inner cortex of the thyroid cartilage indicates a T3 lesion, whereas erosion of the outer cortex of the thyroid cartilage define a T4a tumor. For hypopharyngeal cancer, unlike the larynx, criteria that define T3 lesions are based on vocal cord mobility and tumor diameter only. Hypopharyngeal cancer with invasion of the thyroid or cricoid cartilage indicates a T4a lesion, even in cases of localized cartilage invasion. In any event, accurate staging requires diagnosis of subtle cartilage invasion.

Extralaryngeal tumor spread is also one of the important predictors of T4a disease, with or without cartilage invasion, in laryngeal and hypopharyngeal cancer.

3. Technical considerations for CT, MR imaging and dual-energy CT

3.1. Conventional CT

CT is the preferred imaging method for staging of laryngeal and hypopharyngeal cancer. The images are obtained with the patient supine and during quiet respiration (not while holding the breath). The neck should be in slight extension, and the head is aligned along the cephalocaudal axis to allow comparison of symmetrical structures. Malpositioning may create an appearance that simulates disease. Every effort should be made to make the patient feel comfortable. When a small tumor is suspected, the patient may be scanned during a modified Vasalva maneuver or during phonation to open the piriform sinuses [24,25]. Typically, a 100-mL injection of 300 mgI/mL iodinated contrast medium is injected at a rate of 2.5 mL/s and the scan is initiated 70 s after the start of the injection, proceeding in a cranio-caudal direction. The scan range is set from the base of the skull to the bottom of the neck. Reconstructed images are generated as frontal and coronal sections parallel and vertical to the vocal cords from 1 cm above the hyoid bone to the inferior margin of the cricoid cartilage (2-mm thickness and 16-cm field of view).

3.2. MR imaging

MR imaging is also obtained with the patient supine and during quiet respiration. Axial T2-weighted fast spin echo (FSE) and T1-weighted FSE images are obtained with a scan orientation parallel to the true vocal cords. Typical image parameters for a standard examination include a slice thickness of 3 mm with a 1-mm intersection gap. Additional axial fat-saturated T1-weighted fast field echo (FFE) images after intravenous administration of gadolinium chelates are obtained routinely. When evaluations using CT alone are insufficient to determine cartilage invasion, the following 3D sequences are additionally performed within the area from 1 cm above the hyoid bone to the inferior margin of the cricoid cartilage: a 3D-T2-weighted image (3D-T2WI) is acquired in the transverse plane with a 3D volume isotropic T2-weighted acquisition (VISTA) sequence (TR/TE, 1,100/91 with Driven Equilibrium [DRIVE] technique; flip angle, 90; field of view, 230 mm; matrix, 190 × 448; slice thickness/gap, 1.5 mm/0 mm). A 3D-T1-weighted image (3D-T1WI) is then acquired in the transverse plane with a 3D Turbo Field Echo (TFE) sequence unenhanced (TR/TE, 6/2.3; flip angle,

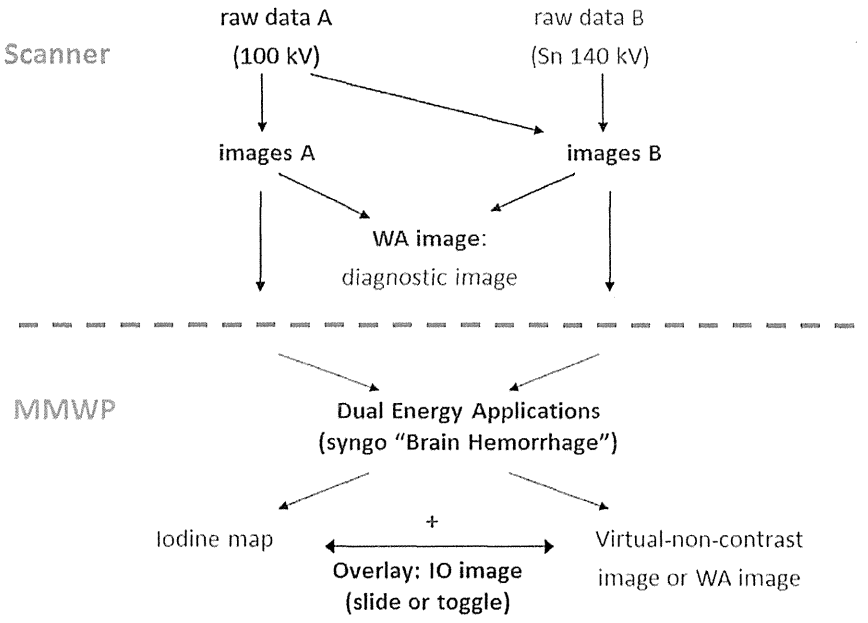

Fig. 1. Flow chart showing an overview of post-processing. Weighted-average (WA) CT images are generated by fusing data sets acquired with different tube voltages (100 and 140 kV). WA images resemble conventional CT images. Iodine overlay (IO) images are generated by fusing virtual non-contrast images and iodine images at a ratio of 0.5.

15; field of view, 230 mm; matrix, 224 × 224; slice thickness/gap, 1.0 mm/0 mm) and fat saturated contrast-enhanced (TR/TE, 6/1.15; flip angle, 15; field of view, 230 mm; matrix, 224 × 224; slice thickness/gap, 1.0 mm/0 mm). Images in the coronal or sagittal plane may be obtained in order to evaluate certain anatomic spaces, such as the preepiglottic space in the sagittal plane, or the paraglottic space and the ventricle in the coronal plane.

3.3. Dual-energy CT

3.3.1. Basic principles

Single-energy CT generates images based on the X-ray absorption coefficient of scanned tissues, and according to their density the tissues are assigned a CT value and displayed as a grey scale. As a result, it may be difficult to differentiate materials of different chemical composition, such as iodine and bone or iodine-enhanced lesions and cartilage, as they have the same CT value on CT images [8,26]. This difficulty can be overcome for some materials using dual-energy CT [15,27,28] which exploits the dependence of the absorption coefficient on the energy of the X-ray spectrum, or kV setting, used for the scan [13,29–31]. For example, materials such as iodine have lower CT values at high X-ray energies than at low X-ray energies, whereas fat tissue shows the opposite behavior. The CT value of water, soft tissue and blood stays almost constant at all X-ray energies.

In practice, two CT images taken at different tube voltages, typically 80 or 100 kV and 140 kV, are sufficient to classify many tissues. Different scan techniques have been developed to acquire dual-energy CT data sets; dual-source dual-energy CT, dual-energy CT with fast kilovolt switching, and multilayered-detector dual-energy CT [32,33]. Here, we limit our discussion to dual-source dual-energy CT [33,34], used at our institution.

Several algorithms can be used to extract material information and generate material maps or remove materials from images. A three-material decomposition algorithm applied to each voxel of an iodine-enhanced dual-energy CT image set makes it possible to compute iodine maps and virtual non-contrast images. Three materials have to be predefined for this algorithm according to the scanned body area: for example iodine, soft tissue and air are chosen for lung imaging [14], and iodine, fat and tissue for liver imaging [33]. For the head-neck region, the materials are set to iodine, brain parenchyma and hemorrhage [12,16].

3.3.2. Dual-energy CT protocol

For dual-source dual-energy CT scans using 128-slice dual-source CT (SOMATOM Definition Flash; Siemens Healthcare, Forchheim, Germany), the following parameters are applied: 100 and 140 kV tube voltages with a 0.4-mm tin filter (labeled as Sn140 kV), 200 and 200 effective mAs, 0.33-s rotation time, 32 × 0.6-mm collimation with a z-flying focal spot, and a pitch of 0.6. The tin filter blocks low-energy X-rays from the 140 kV spectrum, thus reducing radiation to the patient and enhancing energy separation of X-rays from the low and high kV X-ray tubes. These parameters result in an average CT dose index of 14–15 mGy, which is equivalent to that of single-energy CT scans. Noise needs to be minimized to ensure precise three-material decomposition in the head and neck, where many heterogeneous structures such as cartilage, soft tissues and air in the trachea require a high image resolution. A voltage combination of 100 kV and Sn140 kV, rather than 80 and 140 kV, is chosen to minimize noise while maximizing the separation of the X-ray tubes' energy spectra. The methods of contrast material injection are the same as for conventional CT.

3.3.3. Image reconstruction and post-processing

The image reconstruction and post-processing flow is shown in Fig. 1: two sets of raw data (100 kV and Sn140 kV) are separately reconstructed from the acquired dual-energy data using a 1-mm slice thickness and 0.7-mm increment, and a third, WA image set is generated at the same time, linearly weighing and fusing each pixel of the 100-kV and Sn140 kV data (p100 and p140, respectively) at the default ratio of $w = 0.5$ according to the following formula: $[w \times \text{p100}] + [(1 - w) \times \text{p140}]$. A medium sharp D30f kernel is applied for all reconstructions. WA images are used as diagnostic images since they are equivalent in terms of image quality to single-energy 120 kV CT images [35,36].

Next, the images are post-processed on a separate workstation (MMWP; Siemens Healthcare), and three-material-decomposition analysis (Syngo Dual Energy, Brain Hemorrhage; Siemens

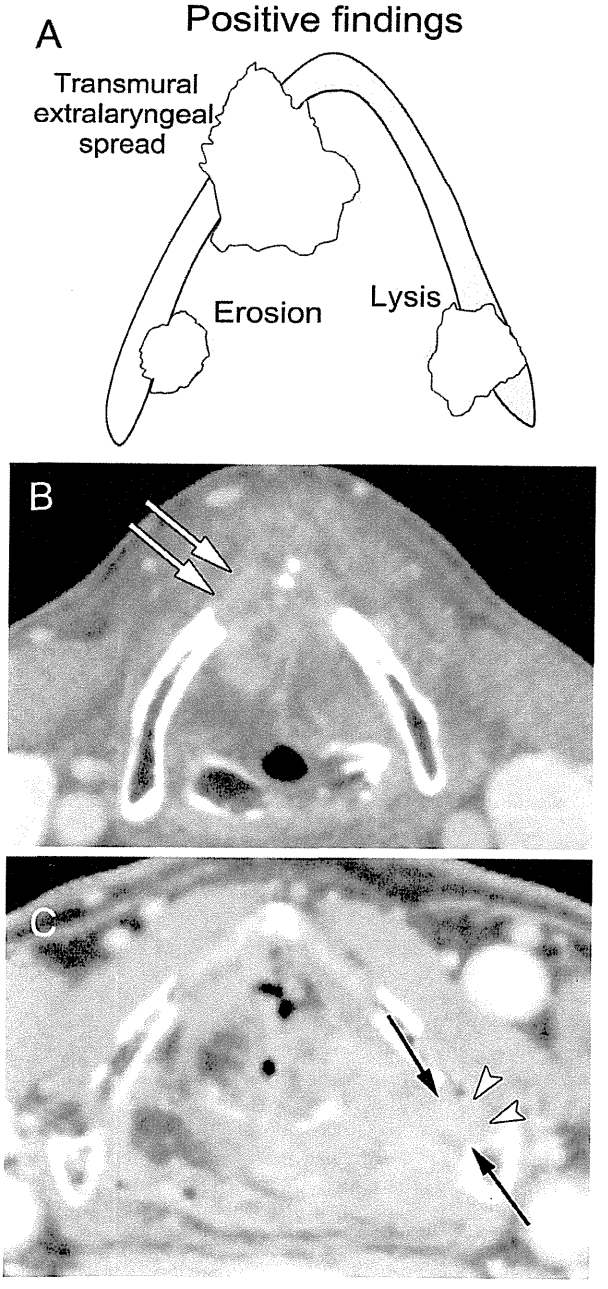

Fig. 2. (A) Drawing to illustrate the criteria for evaluation of thyroid cartilage invasion. Erosion is defined as invasion beyond the inner cortex without reaching the outer cortex (less than half of the cartilage width), lysis is defined as almost reaching the outer cortex but with preservation of the cortex, and extralaryngeal spread is defined as all-layer invasion through both the inner and outer cortex (penetration) of the cartilage, including the extralaryngeal soft tissues. (B) Positive finding of invasion through the outer cortex of the thyroid cartilage in a 56-year-old man with glottic cancer. Axial contrast-enhanced CT image at the level of the vocal cords shows tumor invasion into the thyroid cartilage, spreading into the extralaryngeal soft tissue (white arrows). (C) Positive finding of thyroid cartilage lysis in a 69-year-old man with hypopharyngeal cancer. Axial contrast-enhanced CT image at the glottic level shows a tumor mass arising from the left piriform sinus. The inner cortex of the left thyroid cartilage shows disappearance of a thin hypo-attenuated line between the tumor and the cartilage (arrows), and substitution of cartilage with tumor tissue as demonstrated by CT attenuation (arrowheads).

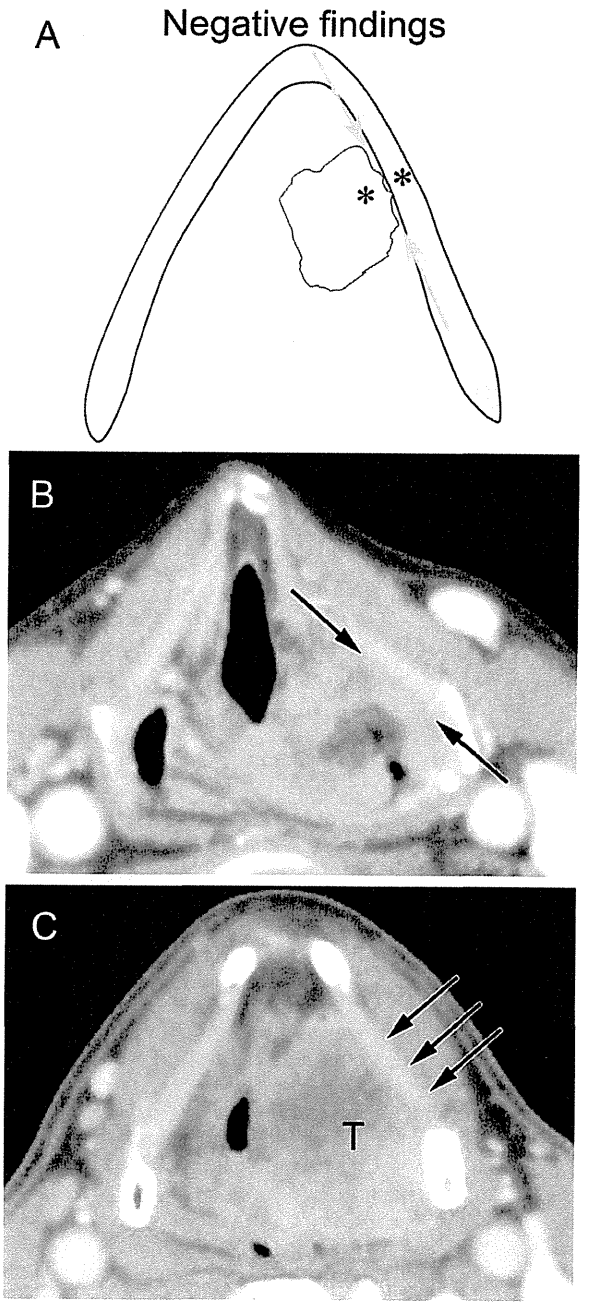

Fig. 3. (A) Drawing to illustrate the criteria for negative thyroid cartilage invasion based on two concurrent findings: (1) perfect or almost continuously defined thin hypo-attenuated line between the tumor and the cartilage (arrows), (2) difference in CT attenuation between non-ossifying cartilage and the tumor (asterisks). (B) Negative finding of thyroid cartilage invasion in a 67-year-old man with hypopharyngeal cancer. Axial contrast-enhanced CT image at the level of the false vocal cords shows a tumor mass arising from the left piriform sinus, but preservation of a dark line between the tumor and the cartilage is evident (arrows). (C) Negative finding of thyroid cartilage invasion in a 61-year-old man with hypopharyngeal cancer. Axial contrast-enhanced CT image at the supraglottic level shows a tumor mass arising from the left piriform sinus. CT attenuation of the non-ossifying cartilage (arrows) is different from that of the tumor (T).

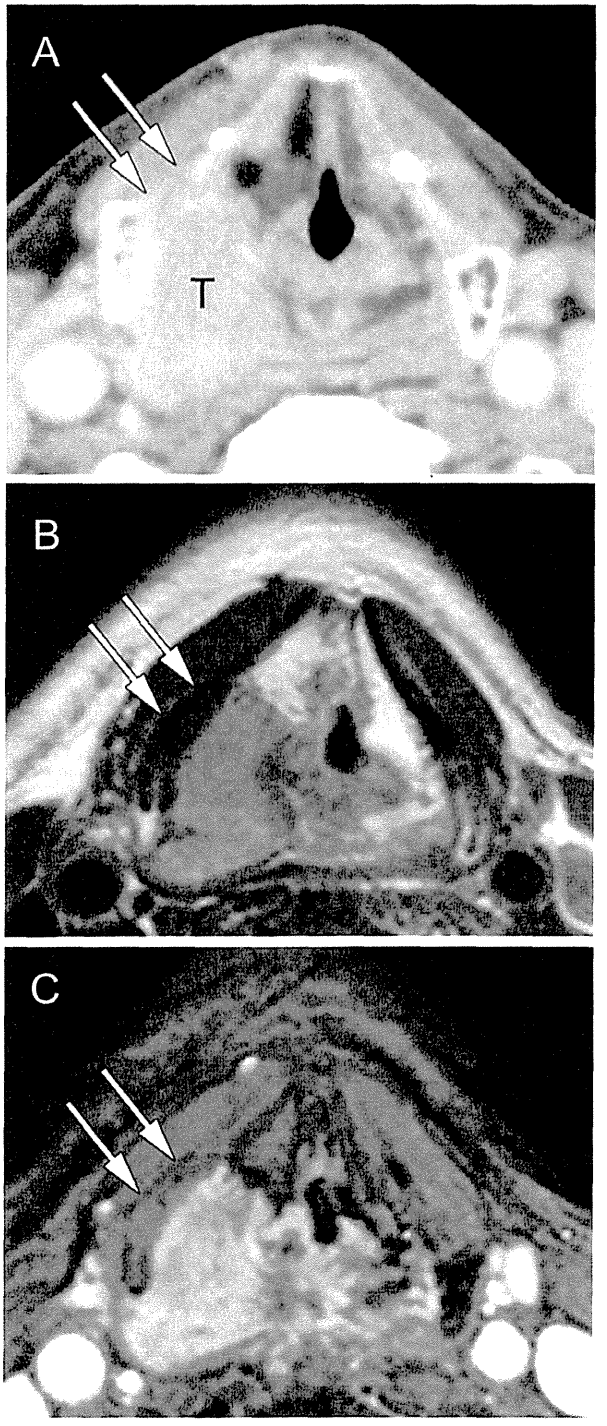

Fig. 4. True negative finding for thyroid cartilage invasion by MR imaging in a 69-year-old man with hypopharyngeal cancer. (A) Axial contrast-enhanced CT image at the level of the false vocal cords shows tumor mass (T) arising from the right piriform sinus. The tumor is located adjacent to non-ossified cartilage of the right thyroid lamina, and the tumor and cartilage show similar CT values, making them almost indistinguishable (arrows). (B) T2-weighted MR image obtained at the same level shows a right-sided piriform sinus tumor with intermediate signal intensity. The adjacent right thyroid lamina can be differentiated by its low signal intensity (arrows). (C) Fat-suppressed contrast-enhanced T1-weighted image shows contrast enhancement of the tumor mass and poor enhancement of the thyroid lamina (arrows) relative to the adjacent tumor mass. Pathological findings confirmed that there was no tumor cell infiltration into the cartilage.

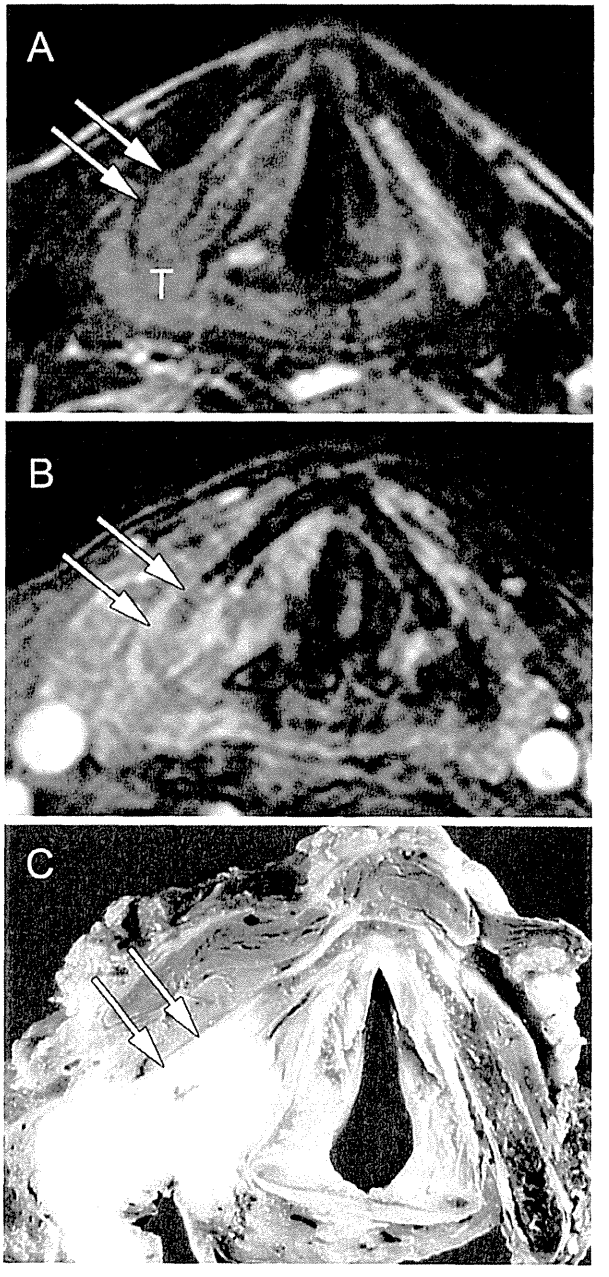

Fig. 5. Positive finding of thyroid cartilage invasion on MR imaging in a 69-year-old man with hypopharyngeal cancer. (A) Axial T2-weighted image at the level of the vocal cords shows a tumor mass (T) arising from the right piriform sinus with intermediate signal intensity. The adjacent right thyroid cartilage shows a similar signal intensity (arrows). (B) Fat-suppressed contrast-enhanced T1-weighted image shows enhancement of the tumor mass and similar enhancement of the adjacent thyroid lamina (arrows). (C) Corresponding axial slice from the surgical specimen at the same level confirms that the posterior thyroid cartilage has been invaded by the tumor cells (arrows).

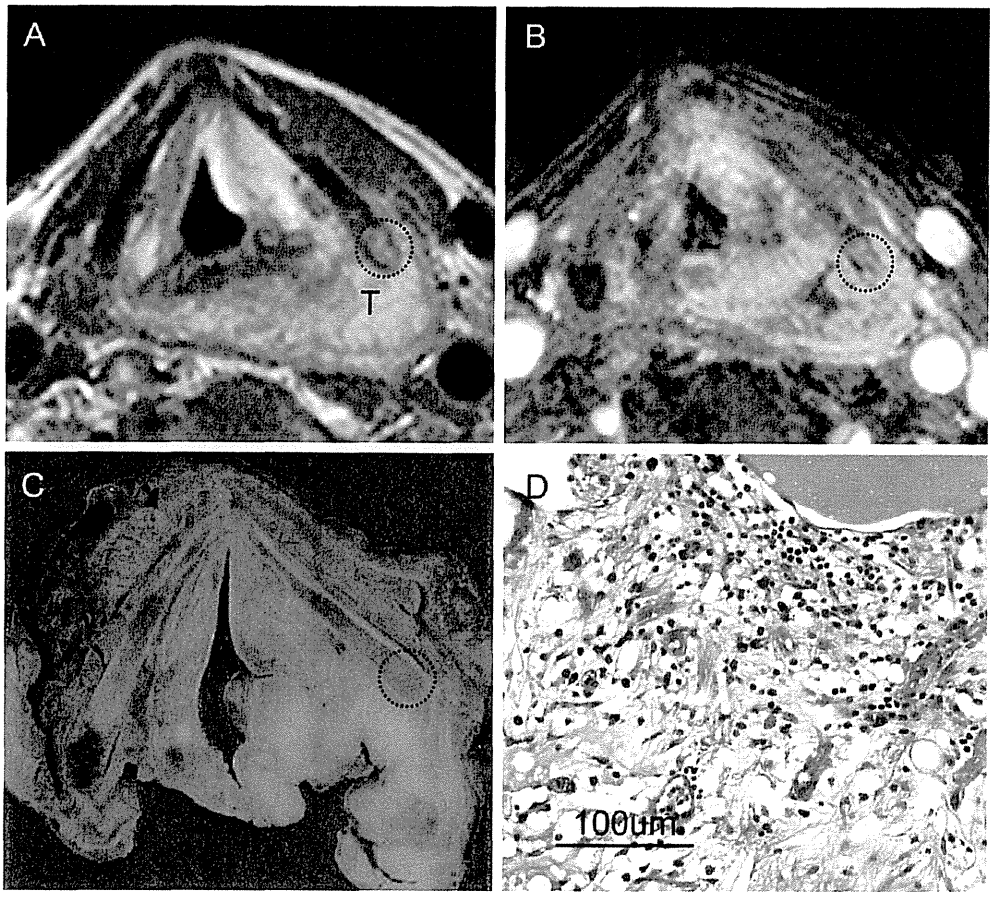

Fig. 6. False-positive findings for thyroid cartilage invasion by MR imaging in a 59-year-old man with hypopharyngeal cancer. (A) T2-weighted MR image at the glottic level shows a tumor mass (T) arising from the left piriform sinus with invasion of the paraglottic space and extension into the soft tissues of the neck. The tumor shows intermediate signal intensity, and the adjacent thyroid cartilage has similar signal intensity (circle). (B) Fat-suppressed contrast-enhanced T1-weighted image shows enhancement of the tumor mass and similar enhancement of the adjacent thyroid lamina (circle). (C) Corresponding axial slice from the surgical specimen at the same level shows that the left thyroid lamina has not been invaded by the tumor (circle). (D) Posterior part of the left thyroid lamina with enhancement (circle in B) shows the moderate infiltration of lymphocytes into the medullary space, accompanied with fibrosis and aggregation of macrophages. (Hematoxylin–eosin stain; original magnification 200×.).

Healthcare) is used to compute iodine images and virtual non-contrast images. The algorithm can be applied at the default parameters for extracting iodine since pharyngeal and laryngeal soft tissues and cartilages have CT values similar to hemorrhage and brain parenchyma. "Organ contour enhancement" and "resolution enhancement" are deselected to ensure quantitative analysis of the small cartilage structures. Finally, the iodine images and the virtual non-contrast or weighted average (WA) images can be linearly fused at a ratio of 0.5, creating iodine overlay (IO) images.

Reconstructed images can then be generated from the WA images and the IO images as frontal and coronal sections parallel and vertical to the vocal cords from 1 cm above the hyoid bone to the inferior margin of the cricoid cartilage (2-mm thickness and 16-cm field of view).

4. Clinical application of CT, MR imaging and dual-energy CT

4.1. Cartilage invasion

Both CT and MR imaging are routinely used for detection of subtle cartilage invasion, but there is still controversy about which modality can most accurately detect cartilage invasion, and both modalities have shortcomings [8,26,37,38]. Dual-energy CT may have the potential to overcome some of the shortcomings of conventional CT, due to the possibility of iodine contrast becoming distributed in tumor tissues but not in normal cartilage. Iodine enhancement can reveal the presence and shape of a tumor, and combined analysis of WA and IO images can be applied to evaluate cartilage invasion. In the next few paragraphs, we discuss the appearances of laryngeal cartilage invasion with conventional CT and MR imaging, as well as dual-energy CT, and explain the advantages and limitations of these modalities.

4.1.1. Conventional CT

Previous studies using single-slice spiral CT scanners have concluded that the CT criteria used for determining neoplastic invasion of the thyroid cartilage include erosion, lysis, and transmural extralaryngeal tumor spread [17,18,26,38,39]. These positive signs of invasion are defined according to the depth of invasion into cartilage, and careful evaluation of the shape and attenuation of the thyroid cartilage (Fig. 2A). In 1997, Becker et al. redefined the diagnostic criteria for single-slice CT and were able to reach an acceptable balance of 71% sensitivity versus 83% specificity by applying these criteria [26]. For evaluation of extralaryngeal spread

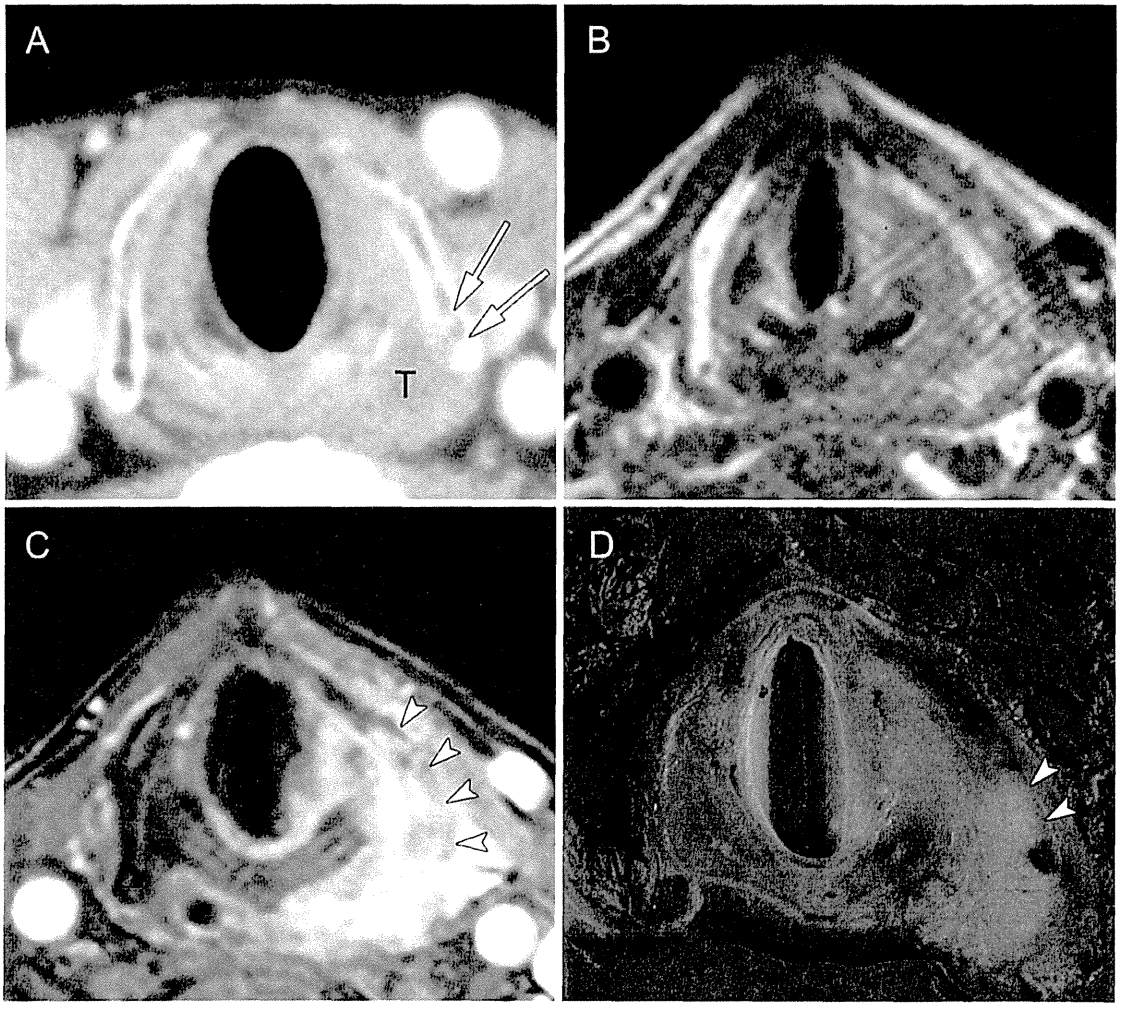

Fig. 7. Hypopharyngeal cancer in a 67-year-old man with thyroid cartilage invasion. (A) Axial contrast-enhanced CT image at the subglottic level shows a tumor mass (T) arising from the right piriform sinus with evidence of focal lysis on the left thyroid cartilage (arrows). (B) T2-weighted MR image obtained at the same level shows a left-sided piriform sinus tumor with intermediate signal intensity. As the motion artifacts are strong, no anatomical information can be obtained in that area and tumor invasion cannot be identified. (C) Fat-suppressed contrast-enhanced T1-weighted image shows more extensive contrast enhancement of the tumor mass and thyroid cartilage than the CT findings. (D) A corresponding slice of the surgical specimen shows the focal infiltration of the tumor into cartilage (arrowheads), consistent with the findings of CT imaging. Thus, the range of tumor cell invasion was overestimated on the fat-suppressed contrast-enhanced T1-weighted MR image.

with cartilage invasion, CT may easily identify tumor growth outside the larynx with cartilage invasion to the soft tissues of the neck (Fig. 2C). This finding is the most reliable criterion of invasion, but is evident only in advanced cases. When determining whether erosion or lysis is present or absent, differentiation from cartilage invasion may sometimes be difficult using conventional CT (Fig. 2B). Some cases may be distinguished from erosion if two concurrent findings of negativity are identified (Fig. 3A): a perfect or almost continuously defined thin hypo-attenuating line between the tumor and the cartilage (Fig. 3B), and CT attenuation of non-ossifying cartilage that differs from that of the tumor (Fig. 3C). However, distortion of adjacent normal structures may mimic tumor involvement, even with careful evaluation.

Asymmetrical sclerosis, defined as thickening of the cortical margin, increased medullary density, or both, when comparing one arytenoid with the other, or one side of the cricoid or thyroid cartilage with the other side, is a sensitive but non-specific feature of cartilage invasion on CT [26,40–42]. For the thyroid cartilage, asymmetric sclerotic changes (ossification) without erosion or lysis should not be diagnosed as positive, as these changes sometimes represent reactive inflammatory changes [26].

The introduction of multi-slice CT has resulted in an increase of spatial and temporal resolution but has led to little progress in interpretation of cartilage invasion [43], which is still sometimes overestimated [9,10]. A fundamental problem of CT is that laryngeal non-ossified cartilage and tumors show similar CT values of about 100 HU, making them almost indistinguishable, especially when the tumor is located adjacent to non-ossified cartilage (Fig. 4A) [8,26]. In addition, the appearance of laryngeal cartilage on CT varies widely according to differences in the proportions of hyaline cartilage (which ossifies with aging), cortical bone, and fatty marrow, which complicates interpretation.

4.1.2. MR imaging

MR imaging seems to be more sensitive than CT for detecting thyroid cartilage invasion (sensitivity up to 96%), as the high contrast resolution of MR makes it possible to detect small areas of marrow space invasion [18,38,44,45]. When assessing cartilage invasion with MR imaging, the T2-weighted and contrast-enhanced T1-weighted signal intensities of the cartilage should be compared with the signal intensities of the adjacent tumor [45]. If the cartilage displays a signal intensity similar to that of the tumor, cartilage

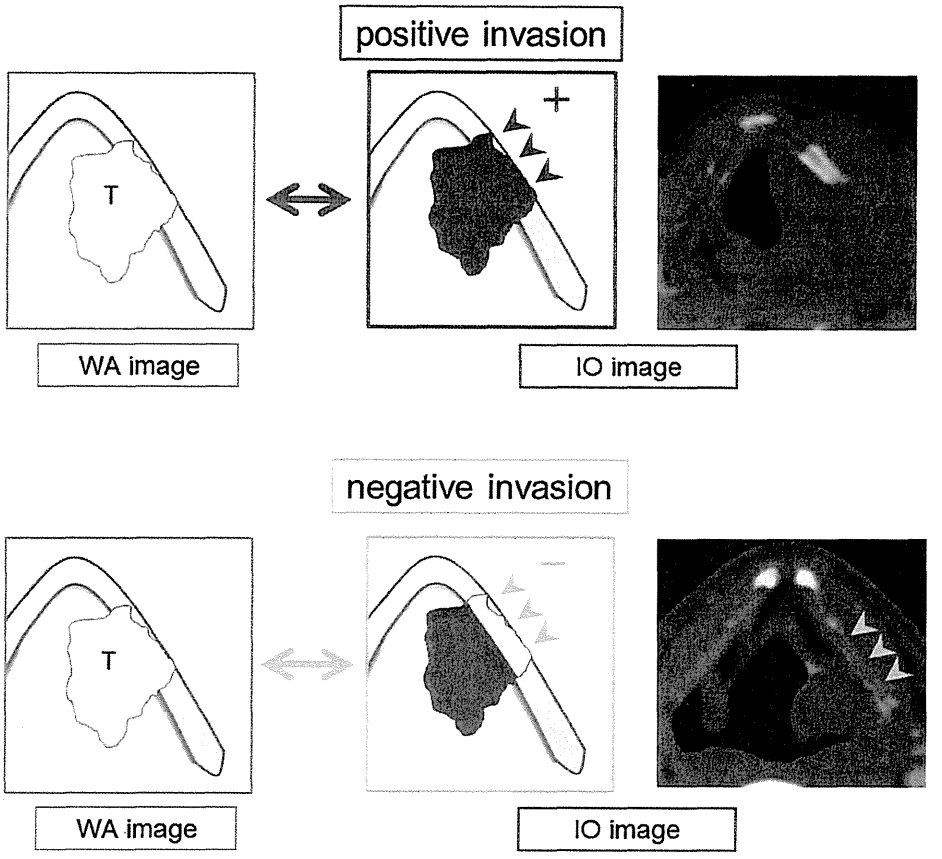

Fig. 8. Criteria for evaluation of cartilage invasion on dual-energy CT WA and IO images.

invasion should be suspected (Fig. 5). Contrast-enhanced MR imaging is also useful when evaluations by CT alone are insufficient for excluding cartilage invasion, and have reached high negative predictive values of up to 96% (Fig. 4) [38,45].

However, the MR findings suggestive of cartilage invasion are not specific, and therefore may lead to a number of false positive signs. The reason is that reactive inflammation, edema and fibrosis in the vicinity of a tumor may demonstrate diagnostic features similar to those of cartilage invasion (Fig. 6). Inflammatory changes are most common in the thyroid cartilage, and therefore the specificity of MR imaging for detecting invasion of the thyroid cartilage is only 56–65% [38,45]. Furthermore, MR resolution is often degraded by motion artifacts [45] and lacks thin sections (Fig. 7B), and the area of tumor extension into cartilage is more easily overestimated on MR imaging than on CT (Fig. 7C). Both of these factors mean that MR imaging is not a satisfactory first choice for imaging of laryngeal and hypopharyngeal cancer.

4.1.3. Dual-energy CT

The recommended dual-energy CT criteria for laryngeal cartilage invasion are summarized in Fig. 8. The IO images are read in addition to the WA images to identify the iodine distribution corresponding to the area displayed on the WA images. After a lesion has been evaluated as positive on WA images, the iodine distribution on the IO images is examined to derive a final classification of either positive or negative. When the IO image shows a corresponding area of tumor cartilage invasion as a red-colored area, positive invasion can be considered based on the combined findings evident on WA and IO images (Fig. 9). When the IO image does not show a corresponding area of tumor cartilage invasion as a red-colored area, tumor invasion can be defined as negative (Fig. 10).

A preliminary report suggests that dual-energy CT has the potential to increase diagnostic performance and reproducibility for evaluation of thyroid cartilage invasion [16]. The reported specificity of combined analysis of WA and IO images obtained with dual-energy CT is significantly superior to that of WA imaging alone (96% vs. 70%) with no compromise of sensitivity (86% vs. 86%), and the interobserver reproducibility of diagnosis using a combination of WA plus IO images is higher than that with WA imaging alone (especially for evaluation of thyroid and cricoid cartilage invasion) [16], and also that reported in a few studies using single-section spiral CT [46,47].

When interpreting the findings of dual-energy CT, it is important to be aware of certain technical limitations. Since this technique applies a 3-material decomposition algorithm with soft tissues and iodine as predefined materials [12,13,33], bone and calcified structures are classified into iodine or soft tissues according to tissue density, and cannot be clearly identified on IO images. As a result, lesions that include calcified structures such as sclerosis and previously ossified parts of cartilage need to be evaluated on WA images first, because on IO images iodine distribution may be overestimated. This does not create an advantage or disadvantage compared to conventional CT, since WA images already have image quality similar to that of conventional CT images. In short, diagnostic reading should always start with the WA image, followed by additional reading of the IO image when appropriate [16].

4.2. Extralaryngeal tumor spread

Extralaryngeal tumor spread is considered to be present when the primary tumor has expanded into extralaryngeal soft tissues, such as cervical soft tissues, the infrahyoid muscles, thyroid gland,

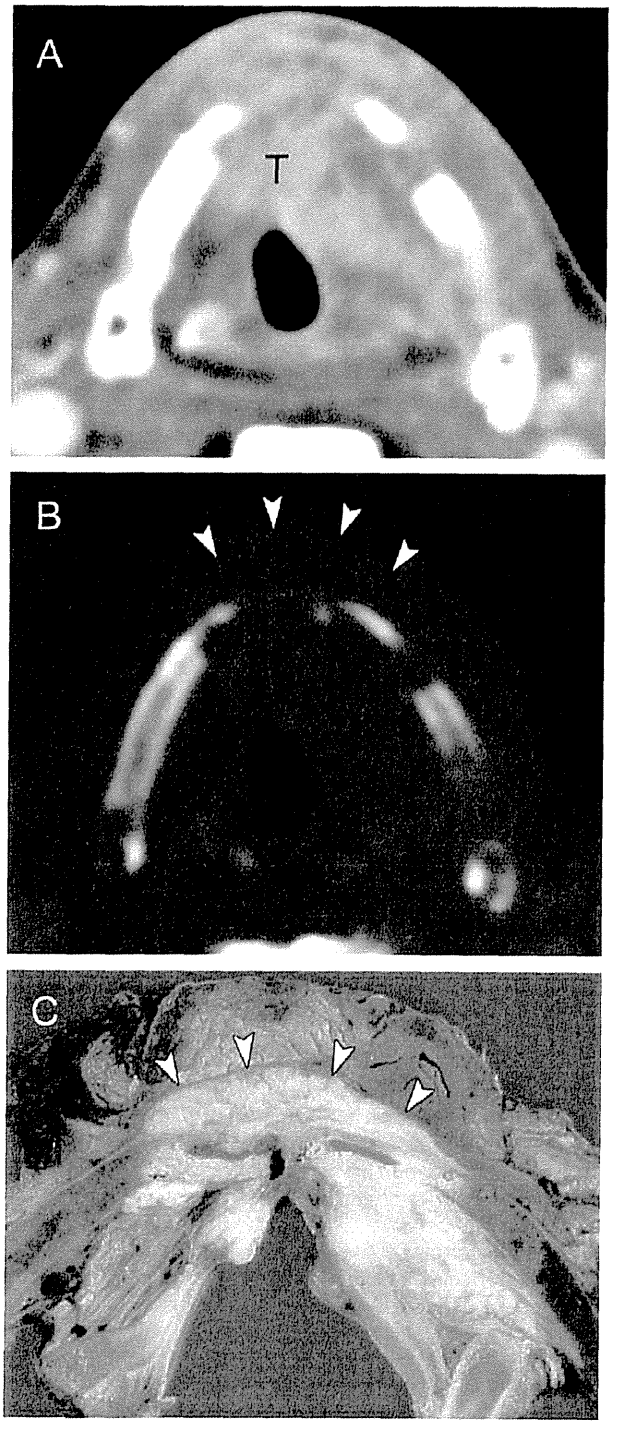

Fig. 9. Positive finding of thyroid cartilage invasion through the outer cortex by dual-energy CT in a 60-year-old man with supraglottic cancer. (A) WA image at the glottic level shows tumor (T) invasion into the thyroid cartilage, spreading into the extralaryngeal soft tissue. (B) On the IO image, the extent of extralaryngeal tumor spread is clearly evident (arrowheads). (C) A corresponding slice of the surgical specimen shows the tumor cell penetrates through the cartilage and invades the extralaryngeal soft tissue (arrowheads), consistent with the findings of the IO image.

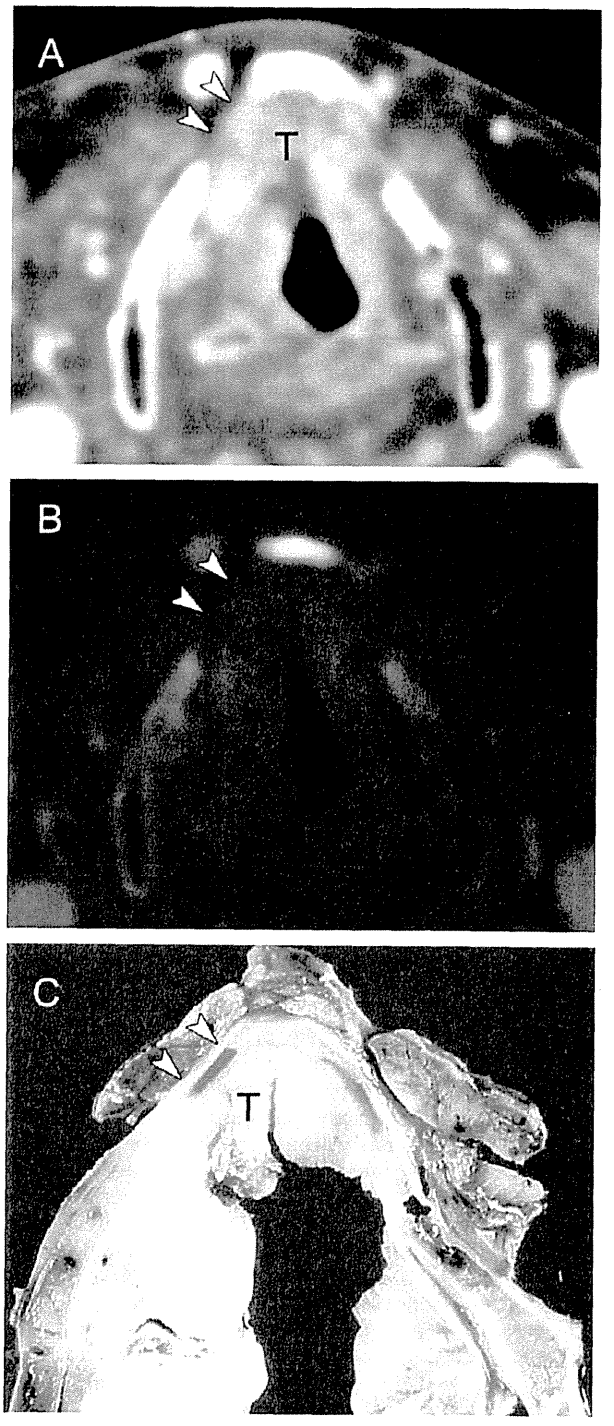

Fig. 10. Negative finding for erosion in the thyroid cartilage by dual-energy CT in a 68-year-old man with glottic cancer. (A) WA image at the level of the vocal cords shows a tumor mass (T) that has invaded the paraglottic space. Non-ossified cartilage of the right thyroid lamina has been substituted by the tumor (arrowheads). (B) IO image clearly shows no corresponding enhancement of the thyroid cartilage (arrowheads). (C) The corresponding slice of the surgical specimen shows that the right thyroid cartilage has not been invaded by the tumor cells (arrowheads).